European Journal of Mechanics / B Fluids 117 (2026) 204443

Contents lists available at ScienceDirect

European Journal of Mechanics / B Fluids

journal homepage: www.elsevier.com/locate/ejmflu

Aerodynamic and aeroacoustic evaluation of slat and slot separation control on a small-scale HAWT: A computational study

Sami Bouterra [a], Riyadh Belamadi [a], Abdelouaheb Djemili [b], Adrian Ilinca [c,*]

[a] National Higher School of Technology and Engineering, Energy Systems Technology Laboratory, LTSE, Annaba 23005, Algeria
[b] Mechanical of Materials and Industrial Maintenance Laboratory LR3MI, Mechanical Engineering Department, Badji Mokhtar University, Annaba, PB 12, Annaba 23000, Algeria
[c] Département de Génie mécanique (Mechanical Engineering Department) École de Technologie Supérieure, Université du Québec, 1100, rue Notre-Dame Ouest, bureau A-1966, Montréal, Québec H3C 1K3, Canada

ARTICLE INFO

Keywords:
Wind turbine blade
Flow separation control
Slat
Slot
FW-H
Aeroacoustics

ABSTRACT

The global push toward clean energy has intensified the search for efficient, innovative technologies to harness renewable resources. Small-scale horizontal-axis wind turbines (HAWTs) offer a promising solution to meet growing urban energy demands with minimal environmental impact. This computational study investigates the aerodynamic and aeroacoustic effects of two passive flow separation control techniques, slat and slot, applied to the blades of a small-scale HAWT. Using the NREL S809 Phase II rotor as a benchmark, simulations are conducted using the steady Moving Reference Frame (MRF) and the unsteady Sliding Mesh Motion (SMM) approaches. The k-ω SST turbulence model is validated against experimental data for multiple inflow conditions. The results demonstrate that flow separation is significantly mitigated by both control methods, particularly at higher wind speeds and at specific locations along the blade span. Quantitatively, the slat and slot configurations yield power output increases of 8.74 % and 21.07 %, respectively, compared to the baseline case. However, aeroacoustic analysis reveals that the slot introduces a sound pressure level (SPL) increase of up to 20 dB near 1 kHz, while providing a more balanced performance in terms of noise and energy gain. These findings highlight the slot configuration as a particularly effective solution for enhancing aerodynamic efficiency, while the slat provides a more balanced aeroacoustic profile. The choice between them involves a trade-off between maximum power gain and noise-control requirements in small-scale wind energy systems.

1. Introduction

Small-scale horizontal-axis wind turbines (HAWTs) are expected to play a growing role in the global clean energy transition, particularly in decentralized and urban energy systems. These turbines are cost-effective, scalable solutions that can serve as backup power sources during outages and be adapted to varying energy demands [20]. As global energy demand rises and reliance on fossil fuels becomes increasingly unsustainable, wind energy emerges as a mature and viable renewable energy option. According to the World Wind Energy Association [44], wind power contributed up to 10 % of global electricity production in 2023, with a 12.5 % increase in installed capacity compared to the previous year. This trend reflects a strong and ongoing push toward larger wind farms and increasing deployment of small-scale HAWTs, particularly in urban and remote areas where grid expansion is challenging.

Enhancing the aerodynamic efficiency of wind turbine blades remains one of the most effective strategies for improving wind energy conversion. Flow separation on the blade surface, particularly at high angles of attack or under unsteady conditions, can lead to performance losses and increased acoustic emissions. These aerodynamic penalties reduce power output and contribute to noise pollution, a significant concern in urban and suburban installations, potentially hindering public acceptance of wind turbines. Thus, power improvement, flow stability through control methods, and noise reduction are fundamental prerequisites for the future expansion of small-scale wind turbines in urban areas.

The NREL S809 Phase II rotor has been extensively studied in both experimental and numerical contexts, serving as a valuable benchmark for exploring flow behavior and control techniques. Foundational

* Corresponding author.
E-mail address: Adrian.Ilinca@etsmtl.ca (A. Ilinca).

https://doi.org/10.1016/j.euromechflu.2025.204443
Received 19 May 2025; Received in revised form 27 November 2025; Accepted 8 December 2025
Available online 9 December 2025

experimental data were provided by Butterfield et al. Butterfield et al., [7], and unsteady RANS simulations were conducted using in-house solvers to examine the effects of turbulence and loading [34]. [13] further extended this work by considering nacelle and tower effects, aiming to validate turbulence models for capturing rotor aerodynamics. A hybrid CFD/BEM approach was proposed by Esfahanian et al. Esfahanian et al., [14] to estimate normal and tangential loads based on 2D sectional lift and drag coefficients. Other studies, such as those of Ali et al. Ali et al., [2], explored morphing trailing edges to enhance power output, while Mostafa et al. Mostafa et al., [29] numerically evaluated the effect of micro-cylinders at the leading edge for separation delay using the k-ω SST model.

Flow separation remains a critical challenge in wind turbine aerodynamics. High lift and low drag are achieved when the airflow adheres to the blade surface [8]. However, adverse pressure gradients near the trailing edge of the suction side can lead to boundary-layer separation, particularly at higher local spanwise angles of attack, resulting in a loss of lift and increased drag. This results in reverse-flow regions and boundary-layer thickening, especially under turbulent or high-load conditions [12].

To mitigate separation and improve performance, passive flow control methods have attracted significant interest due to their energy efficiency and ease of integration. In recent studies, slats and slots, designed to energize the boundary layer and delay flow separation, have been applied to S809 airfoils. Bouterra et al. Bouterra et al., [5] identified optimal slat geometries for separation control and subsequently investigated their aeroacoustic implications for the S809 Phase VI blade using the permeable Ffowcs Williams–Hawkings (FW-H) analogy [43]. Similarly, Belamadi et al. Belamadi et al., [4] assessed the aerodynamic performance of single and double-slot configurations on the S809 Phase II rotor. Despite these advances, the combined aerodynamic and aeroacoustic effects of passive control devices on the S809 Phase II rotor remain insufficiently explored in the literature, particularly under realistic, unsteady flow conditions.

Flow control devices are commonly used to enhance the aerodynamic efficiency and power output of wind turbines by reducing flow separation on the blades' suction surfaces. However, their acoustic impact is also critical, especially considering international noise regulations and the need for public acceptance of wind turbines, particularly in urban or suburban areas.

According to Brooks and Schlinker [6], aeroacoustic sources can be broadly classified into two categories: inflow noise, generated by the interaction between the atmospheric boundary layer and the rotating blades, and airfoil self-noise, which originates from turbulence and boundary-layer dynamics over the blade surface. Consequently, the aerodynamic behavior of the blades is intrinsically linked to the turbine's overall acoustic emission.

The current study focuses on airfoil self-noise, which is directly influenced by the application of flow control devices. The main mechanisms of self-noise generation include:

- Trailing edge noise: caused by the interaction between the turbulent boundary layer and the airfoil's trailing edge.
- Separation noise: induced by unsteady eddies forming in detached flow regions, which alter surface loading distributions [19].
- Tip vortex noise: This noise originates from the pressure differential between the suction and pressure sides at the blade tip, creating strong trailing vortices [31].

Cho et al.'s experimental measurements on a 12 % NREL Phase VI rotor blade with an S809 profile [11] confirmed that noise generation is particularly pronounced near the blade tip and increases with frequency, especially under stalled-flow conditions. Unlike the three-bladed, constant-pitch Phase II rotor, the Phase VI configuration features two tapered and twisted blades, leading to distinct aerodynamic and acoustic behaviors.

In computational aeroacoustics, hybrid methods are often used that decouple the generation and propagation of sound [40]. Near-field aerodynamic data are obtained through unsteady simulations, and the far-field sound is predicted using acoustic-analogy-based models, most notably the Ffowcs Williams–Hawkings (FW-H) equation [43]. In the solid-surface formulation, acoustic sources—such as monopoles and dipoles—are captured via surface integration over a moving control surface coinciding with the blade geometry [38,42].

The FW-H method has been widely adopted for aeroacoustic analysis in various fields, including jet noise, aircraft noise [9], helicopter rotors [24], and wind turbines operating at low Mach numbers for incompressible flow field simulation [27,35,37,41]. Its effectiveness depends on accurately capturing the unsteady flow field, particularly in rotational and turbulent regions responsible for aerodynamic noise. Another FW-H formulation uses a porous surface that encapsulates the rotating blade and captures noise sources. Size and location of the porous surface are essential, and misuse can lead to spurious results. The solid surface was chosen in this study due to its simplicity and its relatively low computational cost compared to the porous surface formulation. Full-scale unsteady simulations, however, are computationally intensive. Consequently, steady RANS–FW-H simulations have been used to compromise aeroacoustic prediction in wind turbine applications.

Two main numerical strategies are generally employed in wind turbine simulations:

- The Multiple Reference Frame (MRF) approach offers a steady-state solution with lower computational cost.
- The Sliding Mesh Motion (SMM) technique offers a more accurate solution for unsteady flows by resolving rotor–wake interactions and turbulence dynamics; however, it is significantly more computationally expensive [20].

Although previous studies [23,36,10] have demonstrated SMM's capabilities for wind turbine analysis, its use remains limited due to its high cost. Nevertheless, SMM is better suited to capturing the unsteady flow structures responsible for aerodynamic noise, particularly when evaluating the impact of flow control strategies.

Despite extensive research on flow control strategies for wind turbine blades, most studies focus on 2D profiles or limited spanwise sections, often neglecting the full 3D aerodynamic and aeroacoustic implications of implementing passive devices such as slats and slots. Additionally, while the aerodynamic performance improvements of these devices have been documented, their influence on far-field noise generation, particularly in unsteady rotating environments, remains insufficiently explored. Furthermore, the comparative assessment of steady (MRF) and unsteady (SMM) approaches for modeling full-rotor performance under flow-control scenarios remains underdeveloped in the literature. This study addresses these gaps by performing a comprehensive 3D computational analysis of the NREL S809 Phase II rotor blade with integrated slat and slot control devices. We use MRF and SMM techniques to investigate the aerodynamic impact and noise emissions under realistic operational conditions. A novel contribution of this work is the aeroacoustic characterization of these control methods using the FW-H analogy, which provides insights into the trade-offs between aerodynamic gains and noise penalties and offers valuable guidance for future low-noise wind turbine blade designs.

The paper is organized as follows. Section 2 outlines the numerical and acoustic methodology, including mesh generation and model parameters. Section 3 presents the MRF-based aerodynamic performance results, followed by transient SMM simulations, flow visualization, and acoustic analysis. Section 4 concludes the study with key findings and perspectives for future work.

2. Methodology

2.1. Turbine description

The NREL S809 Phase II rotor, developed by the National Renewable Energy Laboratory, serves as the benchmark model for this study, which investigates the aerodynamic and aeroacoustic effects of two passive flow separation control devices. This small, downwind, three-bladed horizontal-axis wind turbine (HAWT) features a rotor radius of 5.029 m, as illustrated in Fig. 1. The turbine employs the S809 airfoil profile along most of the blade span. The tower is omitted from this study, which is a limitation as it excludes potential aerodynamic and aeroacoustic installation effects. Its influence will be considered in future higher-fidelity studies, as the focus lies on the aerodynamic performance and flow behavior modifications induced by the passive control methods. The Phase II rotor is characterized by a uniform geometry, with no spanwise twist or taper and a constant chord length of 0.4572 m. The blade uses the NREL S809 profile from 30 % span outward. In comparison, the root region (14.4–30 % span) features a gradual reduction in relative thickness, decreasing linearly from 43 % to 20.95 % chord thickness ratio (t/c) and remaining constant beyond that point [4,7]. Experimental rotor tests were conducted at a rotational speed of 71.68 rpm and a fixed pitch angle of 12°, operating in stall-controlled mode at constant rotational speed [7].

2.2. Control methods definition

Two previously validated flow-separation control techniques, developed through detailed two-dimensional parametric studies, are implemented in the active span region of the NREL Phase II rotor. The key geometric parameters for each method, illustrated in Fig. 2 and summarized in Table 1, correspond to the optimal configurations for each method. The first method employs a slat based on a symmetric E297 airfoil with 0° camber, as validated by Bouterra et al. Bouterra et al., [5]. The second method uses a slot configuration inspired by the work of Riyadh et al. Riyadh et al., [33], which was later enhanced by integrating a leading-edge micro-cylinder and positioning the slot exit at 30 % of the airfoil chord.

This study examines the three-dimensional effects of these passive control strategies on the flow topology over the wind turbine blade, providing a quantitative assessment of power output improvements and the suppression of flow separation. Both steady-state and transient rotational conditions are considered to evaluate aerodynamic performance. Furthermore, the aeroacoustic implications of these three-dimensional control configurations are analyzed by extracting unsteady acoustic pressure data and comparing the results to the baseline (uncontrolled) case.

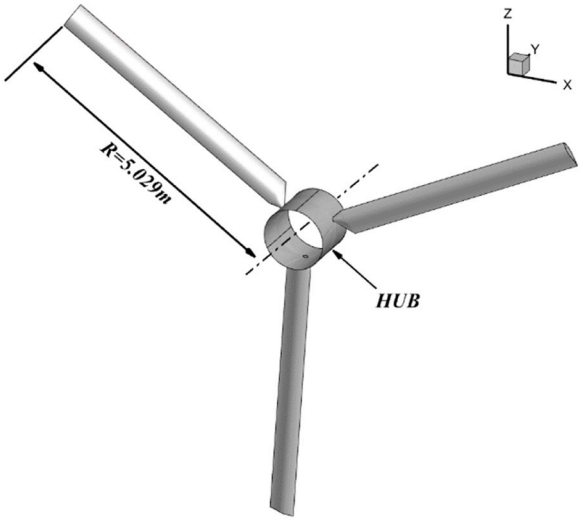

Fig. 1. NREL S809 Phase II rotor.

2.3. Turbulence model

2.3.1. Steady-state simulation

The turbulence model employed in this study is the Reynolds-Averaged Navier–Stokes (RANS) k–ω Shear Stress Transport (SST) model, assuming incompressible, three-dimensional, steady-state flow. This model was selected for its proven ability to accurately resolve turbulent flows in the presence of adverse pressure gradients and boundary-layer separation, key characteristics of wind turbine aerodynamics. The NREL Phase II rotor has been extensively studied using the k–ω SST model, with previous research confirming its reliability in capturing flow separation and delivering accurate predictions of aerodynamic parameters [2,4,14,29,34].

Initially developed by Menter [25], the k–ω SST model combines the strengths of the k–ω formulation near the wall with those of the k–ε model in the free shear layers via a blending function, thereby improving accuracy in transitional and separated flows. Muiruri et al. Muiruri et al., [30] further demonstrated that the k–ω SST model outperforms other RANS models, including the k–ε, k–ε RNG, and Spalart–Allmaras models, in predicting aerodynamic torque and pressure distributions on wind turbine blades. It incorporated a blending function to combine the advantages of the k-ω and k-ε models in the near-wall region and the free shear layer, respectively.

2.4. Grid topology, boundary conditions, and computational approach

2.4.1. Steady-state moving reference frame (MRF)

A multi-block structured mesh was developed for the MRF formulation, as illustrated in Fig. 3. The blade and hub are enclosed within a rotating circular block of thickness 0.2 R and radius 1.4 R. Surrounding this, a static outer block extends 2 R upstream and 10 R downstream, with a radial extent of 3 R. Periodic boundary conditions are applied at the lateral edges of the 120° coaxial domain, enabling the simulation of a single blade and thereby reducing computational costs. The MRF approach reformulates a transient rotating problem into a steady-state one by incorporating additional acceleration terms to account for differences between relative and absolute reference frames. This method is particularly advantageous for providing initial conditions in subsequent transient simulations using the Sliding Mesh (SMM) approach in Ansys Fluent software [3].

A C-type mesh topology is used around the blade profile to capture its complex curvature and ensure high-quality mesh resolution. Mesh refinement is concentrated in critical regions, including the interface between rotating and stationary domains, the blade tip, and the transitional root region ($\Delta x = 0.005$ m), as well as the leading and trailing edges ($\Delta x = 0.0002$ m) and in the downstream wake region ($\Delta x = 0.0005$ m). This localized refinement improves numerical accuracy and enhances solution stability.

Boundary conditions are as follows: a velocity inlet is prescribed at the upstream boundary, and a pressure outlet at the downstream extremity. The blade surfaces and the hub are treated as no-slip walls, while the bottom boundary of the static domain is assigned a slip condition. A symmetry condition is imposed at the upper boundary of the one-third cylindrical domain.

Fig. 4 presents the three-dimensional implementation of the two passive flow control devices applied to the NREL S809 Phase II rotor blade: the slot (Fig. 4a) and the slat (Fig. 4b). Both configurations were previously validated through extensive two-dimensional parametric studies and are here adapted and extruded along the active spanwise region of the blade for full 3D simulation. The slot configuration is integrated into the blade's leading edge, with its exit located at 30 % of the airfoil chord on the suction side, following the design guidelines

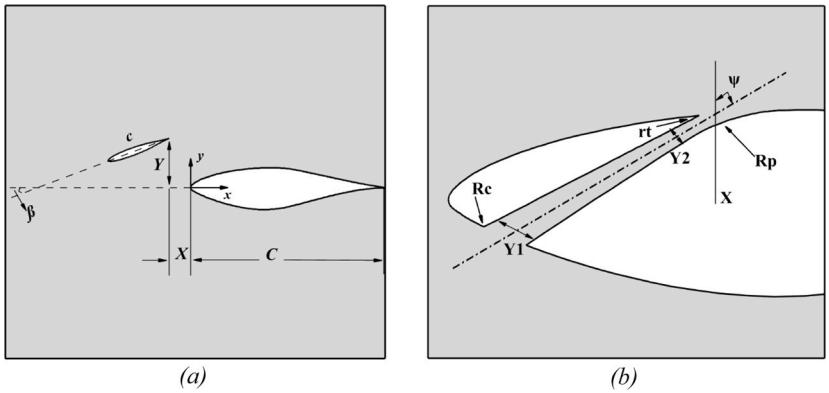

Fig. 2. Geometric parameters for (a) slat and (b) slot configurations.

Table 1
Definition of slot & slat geometric parameters relative to the main element.

SLOT						SLAT			
X: slot location	Y1/Y2: Entrance-Exit ratio	ψ: slot slope	Rp: pressure surface radius	rt: slot trailing edge radius	Rc: Coanda radius	X: horizontal TE position (% of airfoil chord)	c/C: chord length	Y: horizontal TE position (% of airfoil chord)	ß: inclination angle (°)
30 %	3	-60°	100 mm	1 mm	Not defined	3	0.05	4	20

proposed by Riyadh et al. Riyadh et al., [33]. The slat configuration involves placing a secondary symmetric airfoil (E297 profile) at a forward offset from the blade's leading edge, creating a high-velocity passage that energizes the boundary layer and delays flow separation. The geometries are integrated into the blade design to maintain structural continuity and ensure compatible meshing and numerical simulation requirements.

Fig. 5 illustrates the distribution of the non-dimensional wall distance parameter y^+ over the blade surface at various spanwise locations, denoted by the radial ratio r/R. This parameter is crucial for assessing near-wall mesh resolution, particularly in simulations using the RANS approach with the k–ω SST turbulence model. For accurate resolution of boundary-layer and flow-separation phenomena, it is essential to maintain y^+ values within an acceptable range, typically $y^+ < 1$, to ensure that the first grid point lies within the viscous sublayer. As shown in the figure, y^+ values remain below 1 across most of the blade surface, and only a negligible number of cells fall outside this range, confirming the mesh's reliability in capturing key aerodynamic features, including flow separation and reattachment zones critical to the analysis of passive flow control performance.

2.4.2. Sliding Mesh Motion (SMM)

The mesh topology described in the MRF setup is retained for the unsteady simulations using the Sliding Mesh Motion (SMM) approach. SMM provides a time-accurate method for simulating unsteady rotating flows by physically rotating the inner cylindrical block relative to the stationary outer domain. Unlike the MRF method, which uses a steady-state approximation, SMM captures the rotor's transient behavior by allowing the mesh within the rotating zone to move incrementally at each time step. The rotating and stationary domains are connected through conformal mesh interfaces, which are treated numerically as internal boundaries where flow variables are interpolated across the moving surfaces.

Although SMM is computationally more demanding, it provides greater accuracy in modeling rotor–wake interactions and unsteady vortex shedding [32]. All wall boundaries within the rotating zone move synchronously at a prescribed angular velocity. The time step selection is critical in SMM simulations, as it must be smaller than the characteristic time for the fluid to traverse the smallest mesh element to ensure numerical stability and accuracy.

2.4.3. Solver settings

A pressure-based solver was employed for both steady-state and transient simulations, utilizing the SIMPLE (Semi-Implicit Method for Pressure-Linked Equations) algorithm for pressure–velocity coupling. A second-order scheme was applied for pressure discretization, while second-order upwind schemes were used for both momentum and turbulence quantities. Spatial gradients were calculated using a least-squares cell-based method. Under-relaxation factors were slightly reduced to enhance solution stability and promote convergence. The simulation utilized air properties to replicate experimental conditions at 19.1°C, with a density of $\rho = 0.956$ kg/m^3 and a dynamic viscosity of $\mu = 1.7894 \times 10^{-5}$ Pa·s. A low turbulence intensity of 1 % was prescribed at the inlet. The rotational speed is 71.68 rpm, and the pitch angle is 12°.

Convergence was considered achieved when scaled residuals fell below 10^{-5}. For transient calculations, a second-order implicit time-stepping scheme was employed, with a time step of 0.0006 s, as recommended by Sorensen and Michelsen [34]. This time step corresponds to a blade rotation of 0.0036° per iteration, and the total simulated duration covered approximately three and a half full rotor revolutions ($T \approx 2.95$ s).

The blade was initially positioned at the midpoint between the two lateral mesh interfaces in the SMM configuration. To mitigate numerical instability observed in preliminary tests, especially near the blade tip, where curvature gradients and mesh distortion are more pronounced, the upper mesh interface was deliberately offset by 0.4 R vertically above the blade tip. This adjustment ensured smoother mesh motion during rotation and helped prevent divergence caused by excessive sliding-induced shear at the tip.

2.5. Ffowcs-Williams &Hawkings

The fundamental formulation for aerodynamic sound prediction was first introduced by Lighthill [22], who attributed the generation of aerodynamic noise to the inherent unsteady flow structures and instabilities in the fluid. The associated acoustic wave equation is

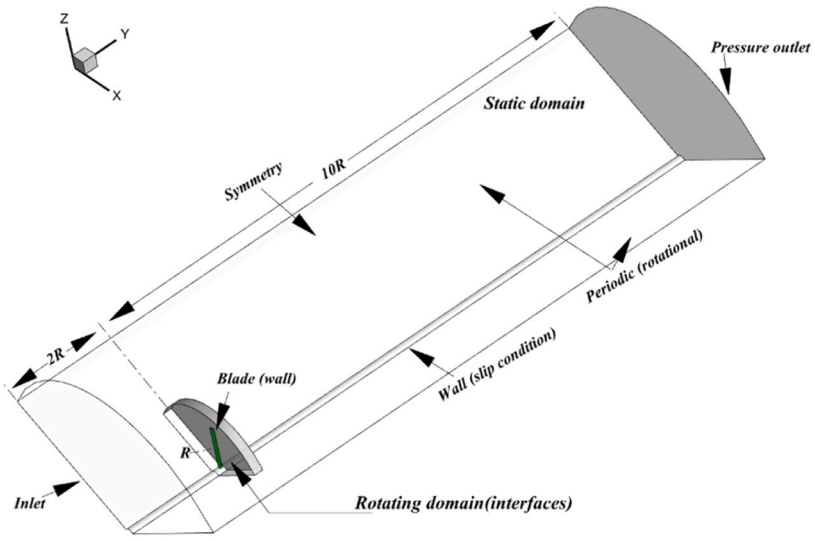

(a)

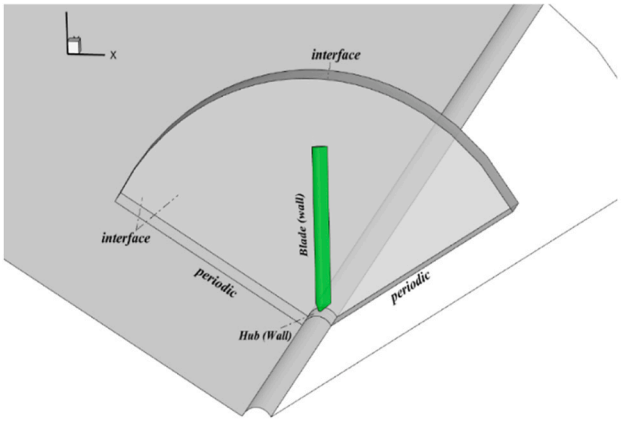

(b)

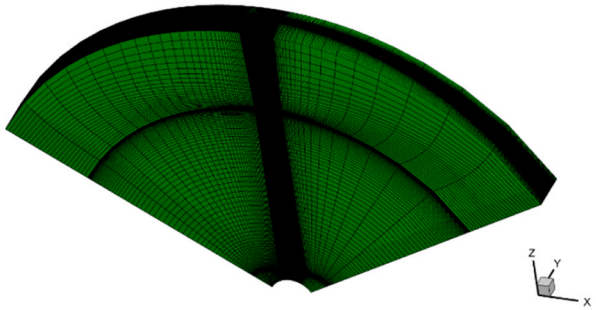

(c)

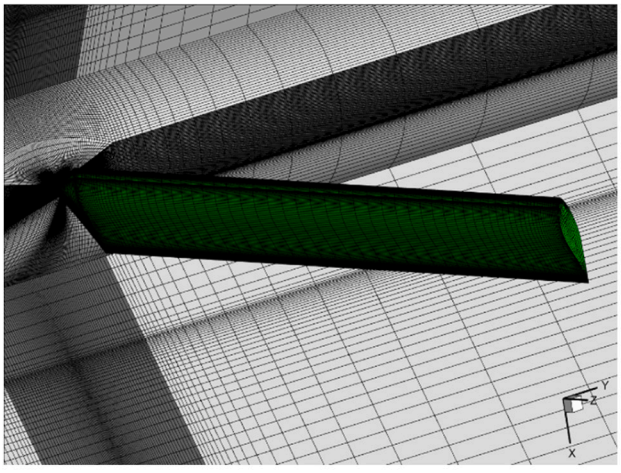

(d)

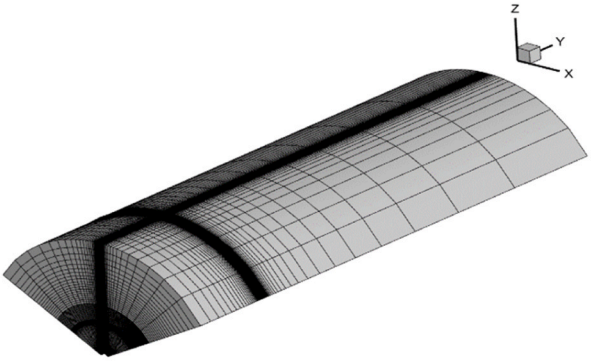

(e)

Fig. 3. Computational domain & mesh details: (a) Full domain boundary conditions, (b) Rotating block BC, (c) Rotating block mesh, (d) Blade mesh, (e) Full domain mesh.

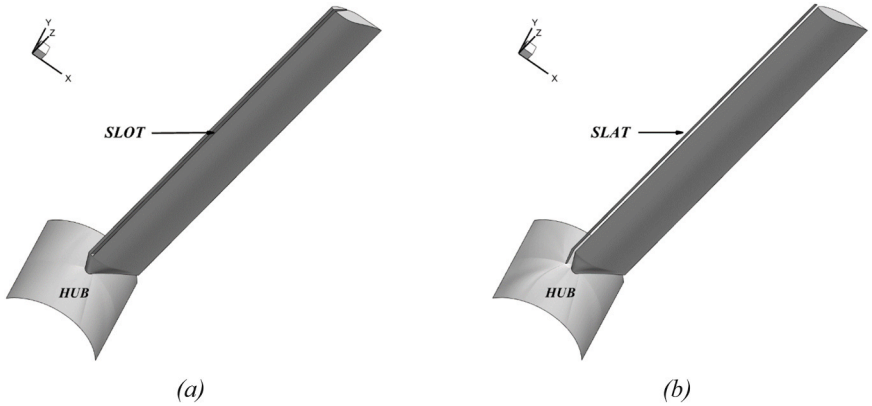

Fig. 4. Slot (a) and slat (b) layout for S809 phase II rotor blade.

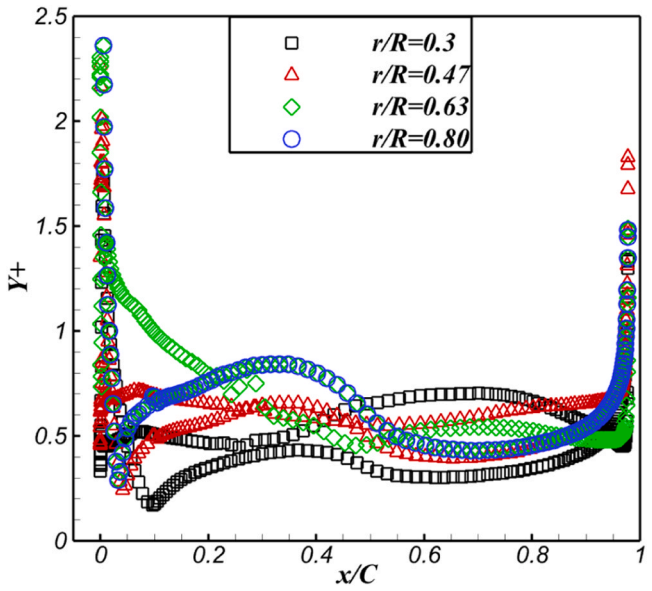

Fig. 5. y + distribution over blade surface (suction & pressure side) at r/R= 0.3,0.47,0.63 & 0.8 for U= 13 m/s.

expressed as:

$$\frac{1}{c_0^2}\frac{\partial^2 p'}{\partial t^2} - \nabla^2 p' = \frac{\partial^2 T_{ij}}{\partial x_i \partial x_j},$$

The right-hand side of this equation describes the wave operator applied to the pressure perturbation $p' = c_0^2(\rho-\rho_0)$, and $T_{ij} = \rho u_i u_j + P_{ij} - c_0^2(\rho-\rho_0)\delta_{ij}$, where $\rho u_i u_j$ are convection forces represented by the Reynolds stresses, P_{ij} is the viscous stress tensor, c_0 is the sound speed, and represents the speed at which disturbances travel in the flow.

To account for the sound generated by moving solid bodies, such as rotating wind turbine blades, the (FW-H) equation was developed [43]. This extension introduces generalized functions, specifically the Heaviside function *H(f),* and captures the acoustic influence of moving solid surface bodies as sound sources. It is derived by manipulating the continuity and momentum equations into an inhomogeneous wave equation [15]. In the acoustic medium, the identification of the blade's solid surface (non-penetrating condition) and its motion is achieved by using a function f (x, t) that satisfies f(x,t) = 0 at the surface, f < 0 inside the surface, and f > *0* outside the surface. The blade surface is equivalent to the acoustic source surface (wall boundary condition). The differential FW-H equation valid both inside and outside of f is obtained using the Heaviside function: $H(f) = \begin{cases} 1 & \text{if } \begin{cases} f > 0 \\ f < 0 \end{cases} \\ 0 \end{cases}$, and Dirac's delta function defined by: $\frac{\partial H(f)}{\partial f} = \delta(f) = \begin{cases} \infty & \text{if } \begin{cases} f = 0 \\ f \neq 0 \end{cases} \text{ to yield;} \\ f \end{cases}$

$$\frac{1}{c_0^2}\frac{\partial^2 p'}{\partial t^2} - \nabla^2 p' = \frac{\partial}{\partial t}[(\rho_0 v_n)\delta(f)] - \frac{\partial}{\partial x_i}[l_i \delta(f)] + \frac{\partial^2}{\partial x_i \partial x_j}[T_{ij} H(f)],$$

This equation describes the propagation of sound by three discernible sources:

- The first term on the right represents a monopole source and is defined as a mass flow rate time derivative, v_n is the surface velocity in the outward direction.
- The second term contains the local force vector, $l_i = p'_{ij} n_i$, and represents the sound source produced by viscous stresses and the aerodynamic pressure exerted by the surface on the fluid [39]. n_i is the outward surface normal unit vector. It is characterized as a dipole source term due to the surface-over-fluid effect.
- The last term contains $H(f)$ which is valid outside f. Therefore, it represents a volume source or quadrupoles and is mainly due to turbulence.

The surface and volume sources integration in the above equation is carried out utilizing Green's function:

$$G(x,t;y,\tau) = \begin{cases} 0 \\ \delta(g)/4\pi r \end{cases} \text{ if } \begin{cases} \tau > t \\ \tau \leq t \end{cases}, \; g = \tau - t + r/c_0, \; r = |x - y|$$

The resolution of the classical formulation of the FW-H equation allows for the estimation of the emitted source sound (coordinate: y at time: τ) perceived by a receiver at coordinate: x at time: t. At low Mach number, the contribution of volume source (Lighthill's tensor) is considered negligible compared to both surface terms [16]. Thus, the acoustic pressure has two components $p' = p'_T(x,t) + p'_L(x,t)$, p'_T and p'_L are the thickness and loading noise respectively:

$$4\pi p'_T(x,t) = \& \int_{f=0} \left[\frac{\rho_0(\dot{v}_n + v_{\dot{n}})}{r(1-M_r)^2}\right]_{ret} dS$$

$$\& + \int_{f=0} \left[\frac{\rho_0 v_n (r M_i r_i + c_0 M_r - c_0 M^2)}{r^2(1-M_r)^3}\right]_{ret} dS$$

$$4\pi p'_L(x,t) = \& \frac{1}{c_0}\int_{f=0} \left[\frac{\dot{l}_i r_i}{r(1-M_r)^2}\right]_{ret} dS$$

$$\& + \int_{f=0} \left[\frac{l_r - l_i M_i}{r^2(1-M_r)^2}\right]_{ret} dS$$

$$\& + \frac{1}{c_0}\int_{f=0} \left[\frac{l_r (r M_i r_i + c_0 M_r - c_0 M^2)}{r^2(1-M_r)^3}\right]_{ret} dS$$

In this study, aeroacoustic predictions using the FW-H acoustic analogy are performed during the final full rotation of the unsteady

SMM simulation, once the flow field is fully developed and stabilized. The no-slip wall surfaces of the blade, especially the tip and suction side, serve as primary acoustic source surfaces in the baseline configuration.

For the controlled configurations, the internal surfaces of the slat and slot flow control devices are also included as acoustic source contributors.

Acoustic pressure data from these surfaces is post-processed using the Fast Fourier Transform (FFT) to obtain frequency-domain sound pressure levels (SPLs) at designated receiver locations. To avoid reflections, the domain was larger than the minimum required for the sound source, which was placed one wavelength away from the domain boundaries. Before the FFT, the unsteady pressure signals were detrended and multiplied by a Hanning window to reduce spectral leakage, and then the SPL spectra were computed.

To evaluate the directivity of the acoustic emission, 36 equally spaced receivers are positioned circumferentially around the rotor at ground level, forming a circular arc at a radius equal to the blade length (Fig. 6a). The receiver distance complies with the IEC 61400–11 standard, placing the far-field sensors at a horizontal distance of H + D/2 from the rotor center (where H is the hub height and D is the rotor diameter). This setup enables quantification of directivity and SPL variation around the turbine for each configuration.

3. Results and discussion

In this section, the results obtained from the steady-state MRF simulations are validated against available experimental data and previous numerical studies. To assess the aerodynamic performance and the effect of the passive control methods, three uniform inflow velocities, U = 7 m/s, 13 m/s, and 19 m/s, are imposed at the domain inlet. The aerodynamic coefficients and power output are analyzed for both the baseline and controlled configurations.

In addition to steady-state validation, the reliability of the unsteady SMM approach is confirmed through torque predictions, which are compared with benchmark values to assess the accuracy of the transient aerodynamic simulations.

Moreover, the aeroacoustic behavior of the turbine is evaluated across all configurations using the FW-H acoustic analogy, with special attention to the impact of control methods on far-field noise emissions. Although aeroacoustic experimental data for the NREL S809 Phase II rotor are not publicly available, limiting the direct validation of noise predictions, the aerodynamic validation methodology adopted in this study follows established practices used in similar investigations, such as those of [21,28,41].

3.1. Mesh independence

In this section, the simulation results' independence from the grid size is assessed by comparing experimental power values. Table 2 summarizes the key parameters used for mesh sensitivity analysis (the error percentage is defined as the relative deviation of the computed power from the corresponding experimental measurement at each wind speed), focusing on their influence on computed power output and the associated relative error compared to experimental measurements. The mesh independence study was conducted for the baseline blade configuration under three uniform inflow velocities: 7 m/s, 13 m/s, and 19 m/s. The analysis considered variations in the first cell height adjacent to the wall and in the number of chordwise and spanwise elements across four mesh densities (G1 to G4).

Results indicate that mesh parameters significantly affect predicted power values. At 7 m/s, all four mesh configurations yielded relatively similar power errors, with G4 exhibiting the lowest deviation from experimental data. While G1 produced the smallest error at 19 m/s, it notably overpredicted power at 13 m/s, a critical velocity for the onset of separation. In contrast, G2, G3, and G4 demonstrated consistent and more accurate results across all wind speeds.

Based on this consistency and better convergence of the deviation between experiment and simulation at 13 m/s, G4 was selected as the optimal mesh for all subsequent simulations. A growth factor of 1.1 was applied, and the resulting y^+ distribution, presented in Fig. 5, shows values close to unity, aligning with recommended practices for the k–ω SST turbulence model and providing an accurate resolution of the viscous sublayer [26].

It is important to note that the same mesh generation methodology was extended to the slat and slot configurations to ensure compatibility with the validated baseline grid. Specifically, 40 chordwise elements were used on both the pressure and suction surfaces, as well as on the inner walls of the slot geometry, to maintain high resolution near critical flow features. Discrepancies between experimental and numerical results are further discussed in Section 3.2. The number of chordwise cells near the interface (stationary/moving block) per minimum wavelength of interest corresponding to 1 kHz is around 40.

3.2. Model validation

To validate the steady-state numerical model, pressure coefficient C_P distributions were compared against experimental data obtained from the well-documented campaign by Butterfield et al. Butterfield et al., [7]. Pressure tap measurements were taken at four spanwise stations along the blade, r/R = 0.30, 0.47, 0.63, and 0.80, for three steady-state inflow speeds (U = 7 m/s, 13 m/s, and 19 m/s). In addition, numerical

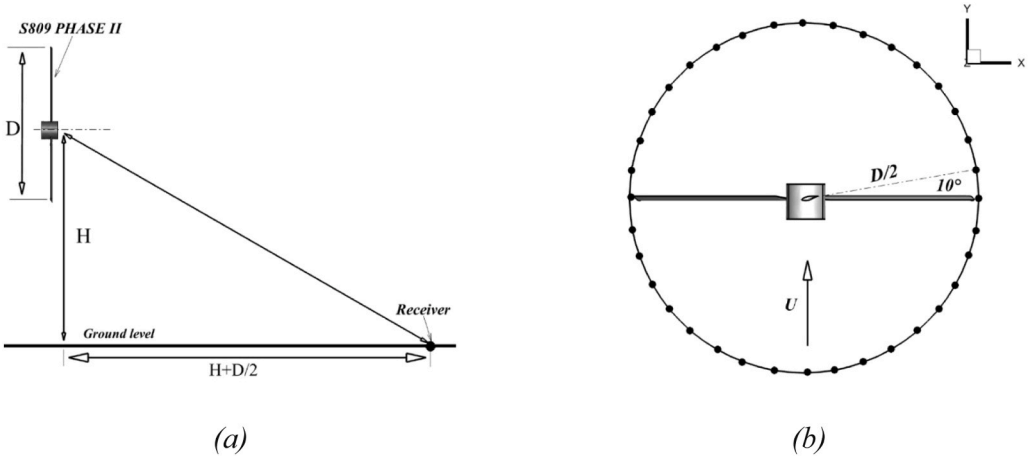

Fig. 6. Acoustic receivers layout: (a) SPL receiver, (b) Directivity receiver (top view).

Table 2
Grid independence study.

	N° elements*10^6			Airfoil			Computed power (kW)					
	total grid number	Inner domain	Outer domain	Wall adjacent cell (m)	N° of chordwise elements	N° of spanwise elements	7 m/s	Error (%)	13 m/s	Error (%)	19 m/s	Error (%)
G1	1.7	0.8	0.9	0.002	90	60	1.170	53,93	16.716	28,88	19.963	7,32
G2	3.3	1.8	1.46	0.00002	140	80	1.880	25,98	11.866	8,51	16.308	12,32
G3	3.6	2.1	1.46	0.00002	80	100	1.907	24,92	16.670	10,02	15.315	17,66
G4	4	2.3	1.7	0.00001	140	120	2.010	20,86	11.881	8,39	15.535	16,47

results from Sorensen & Michelsen [34] and Belamadi et al. Belamadi et al., [4] were included for comparative purposes.

As shown in Figs. 7, 8, and 9, a relatively good agreement was achieved between the present simulation and both experimental and previously published numerical results at r/R = 0.47, 0.63, and 0.8. The model accurately captured the pressure-coefficient trends on both the suction and pressure sides at these stations for all three inflow speeds.

However, noticeable discrepancies emerged in the root region (r/R = 0.3), particularly on the suction side. While the pressure-side predictions remained consistent with the experimental data, the suction-side predictions exhibited significant deviations, especially from the leading edge to mid-chord. This divergence becomes more pronounced at higher inflow speeds.

At U= 13 m/s, the deviation in predicted C_p values increased to approximately 71 % at r/R= 0.30 and 40 % at r/R= 0.47, spanning nearly the entire suction surface. This trend suggests a clear correlation between rising wind speeds and the growth of flow separation, particularly in the near-root region where adverse pressure gradients are strongest, and the RANS model struggles to capture complex 3D separation dynamics.

For r/R= 0.63 and 0.80, the simulation maintained good predictive accuracy even at higher speeds, confirming the model's reliability in mid-span and near-tip regions (Fig. 8). At the highest tested wind speed, U = 19 m/s, deviations became more pronounced across all four spanwise stations, with the suction side again exhibiting the most significant errors. At r/R= 0.30, the deviation reached up to 70 %, as shown in Fig. 9. Overall, the spanwise C_p distribution is explained by the effect of separated flow under high angles of attack. The above results correlate with the values in Table 2, as the discrepancies in power can be attributed to lift loss in spanwise portions of the blade. Belamadi et al. [4] and Sorensen and Michelsen [34] similarly attributed C_p discrepancies to high local angle of attack, especially near the root region. The primary difference lies in the use of in-house code, as noted by Sorensen and Michelsen [34].

These results confirm that while the k–ω SST RANS model performs robustly in the mid-span and tip regions, it exhibits limitations in

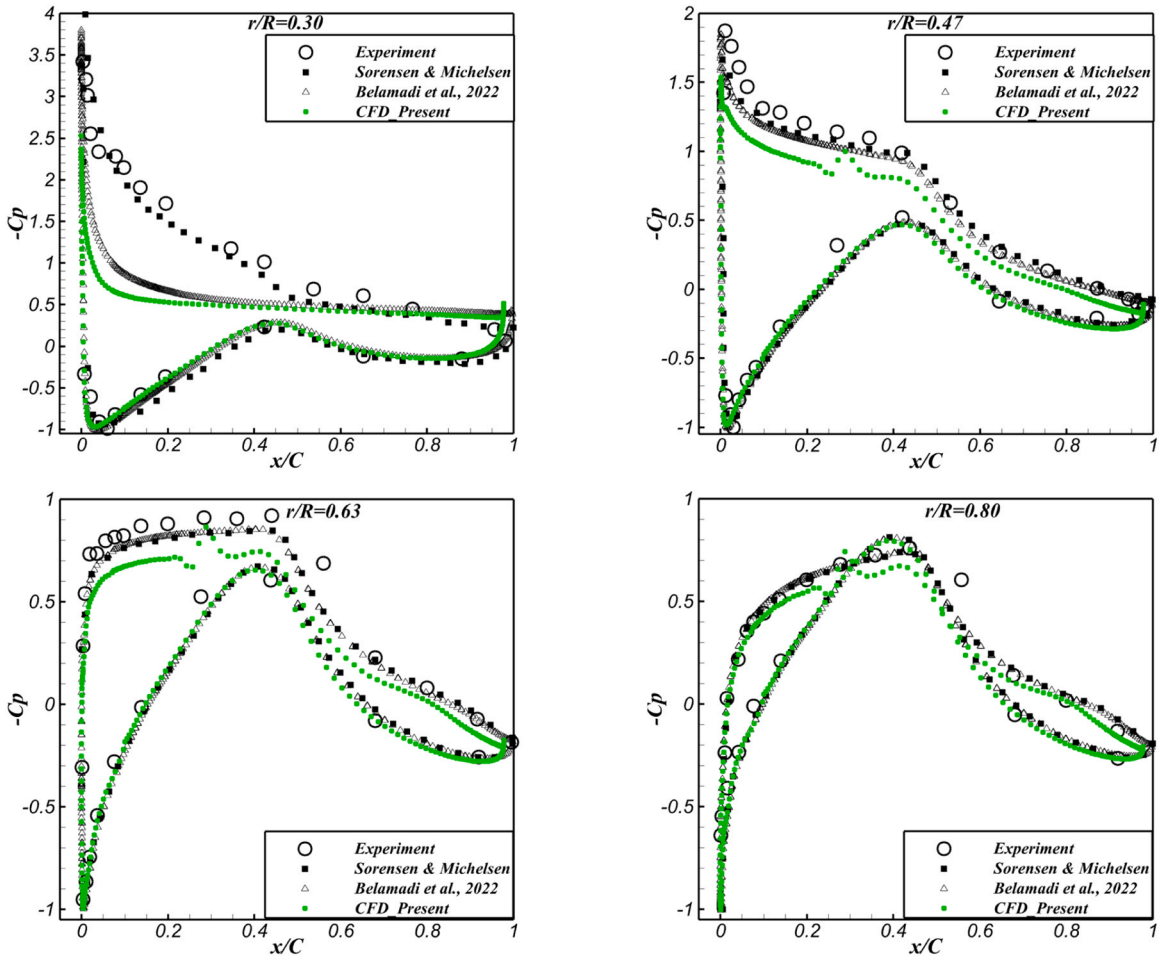

Fig. 7. Comparison of pressure coefficient distribution for spanwise stations r/R= 0.3, 0.47,0.63 & 0.8 at 7 m/s.

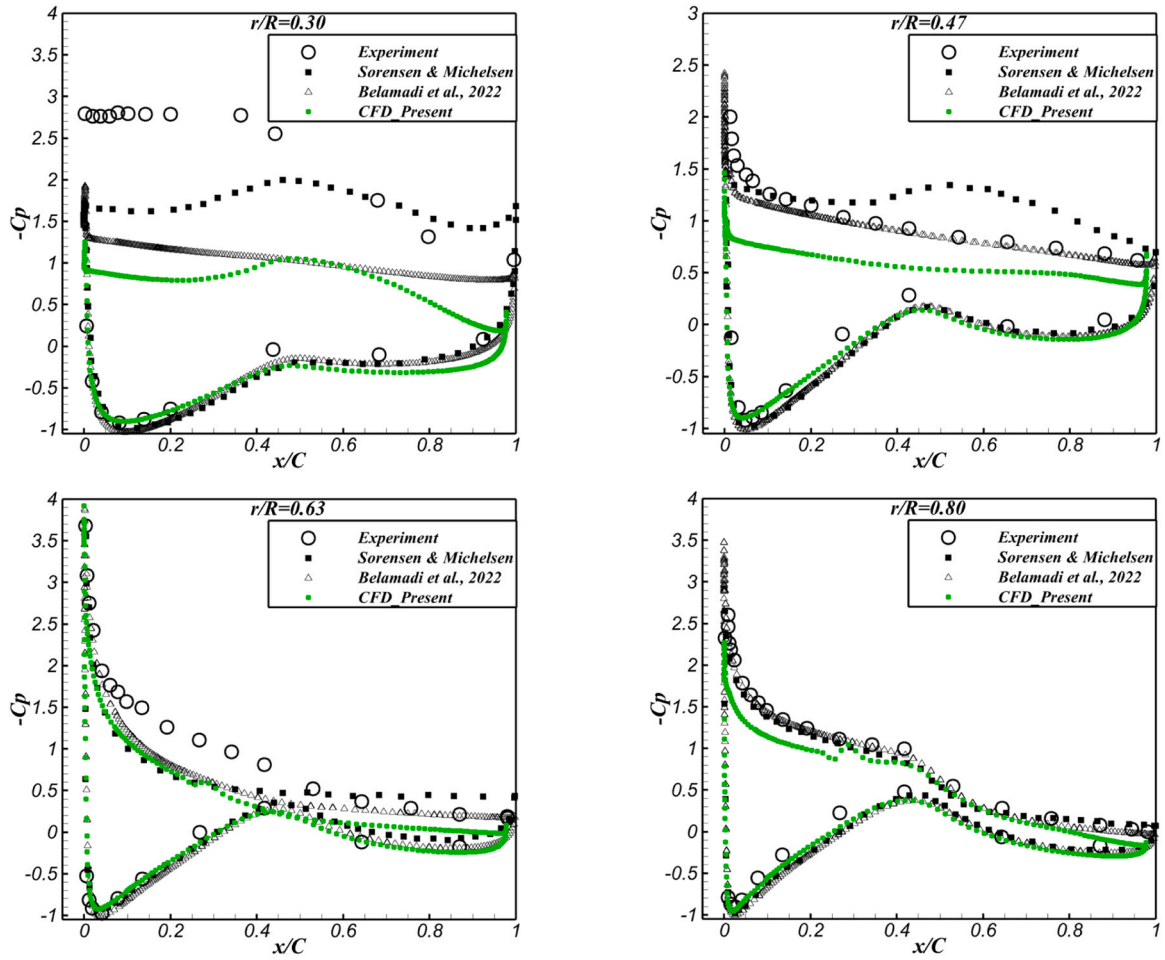

Fig. 8. Comparison of pressure coefficient distribution for spanwise stations r/R= 0.3, 0.47,0.63 & 0.8 at 13 m/s.

capturing strong separation near the blade root, particularly under high inflow conditions. This underscores the potential value of higher-fidelity approaches (e.g., LES or hybrid RANS/LES) for future investigations focused on near-root dynamics.

3.3. Aerodynamic and performance evaluation of control methods using MRF

3.3.1. Velocity streamlines and pressure contours

For the slot and slat configurations, steady-state velocity streamlines and pressure contours were examined and compared to the baseline configuration to assess the aerodynamic effects of the two passive flow control methods. These visualizations were generated at four spanwise stations (r/R = 0.30, 0.47, 0.63, and 0.80) for three uniform inflow velocities (7 m/s, 13 m/s, and 19 m/s), as shown in Figs. 10–12.

At the lowest inflow velocity (7 m/s) (Fig. 10), a pronounced separation bubble develops over the suction side at r/R= 0.30 in the baseline configuration, extending to nearly half the chord length. In contrast, both the slot and slat configurations effectively suppress the separation at this critical near-root location. This highlights the effectiveness of the control devices in managing flow detachment at low speeds.

Notably, both control methods also modify the leading edge pressure distribution. In the slot configuration, the low-pressure zone is elongated downstream of the slot jet exit, driven by the accelerated, re-energized flow. For the slat configuration, a strong low-pressure region forms on the suction side of the slat itself, contributing to a more extensive low-pressure area near the blade's leading edge.

The flow remains essentially attached across all configurations for the remaining spanwise stations (r/R = 0.47, 0.63, and 0.80). While separation is not observed at these stations, the pressure contour topologies differ significantly between cases. The slot configuration introduces a distinct secondary low-pressure region at the slot jet exit, particularly evident at higher inflow velocities. In the slat configuration, for instance, at r/R = 0.47, a slightly deeper depression zone forms on the suction side (resulting in a higher fluid velocity). The depression zones tend to extend either chordwise along the blade surface or vertically, perpendicular to the wall, depending on the spanwise location and inflow speed.

These differences in streamline behavior and pressure field distribution suggest that each control method alters local aerodynamic behavior differently, with the slot acting more as a boundary-layer energizer and the slat contributing to flow stabilization and lift enhancement.

Flow separation becomes more prominent at an inflow velocity of 13 m/s (Fig. 11), especially in the baseline configuration. The streamlines detach from the leading edge and form a large recirculation zone that extends over the entire blade chord at r/R= 0.30 and 0.47. When the slot is introduced at r/R = 0.30, it disrupts the continuous separation by splitting the large recirculation zone into two smaller, less intense detached regions located fore and aft of the slot. Although separation remains, the depression zone behind the slot is less severe than in the baseline case, indicating partial suppression of adverse pressure buildup.

In the slat configuration, while separation persists at r/R= 0.30, the enhanced suction effect generated by the convected flow over the slat's surface amplifies the local low-pressure zone near the blade wall. At r/R

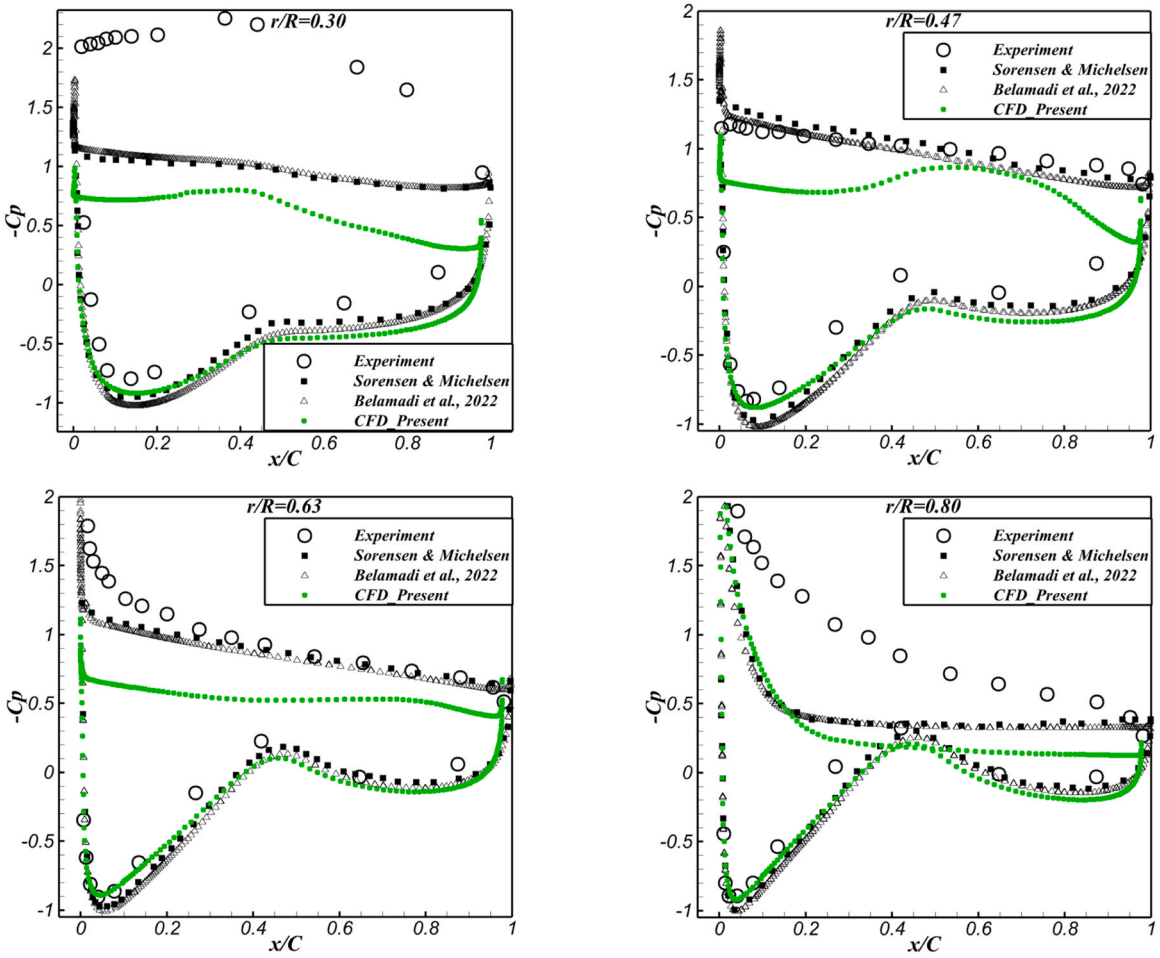

Fig. 9. Comparison of pressure coefficient distribution for spanwise stations r/R= 0.3, 0.47,0.63 & 0.8 at 19 m/s.

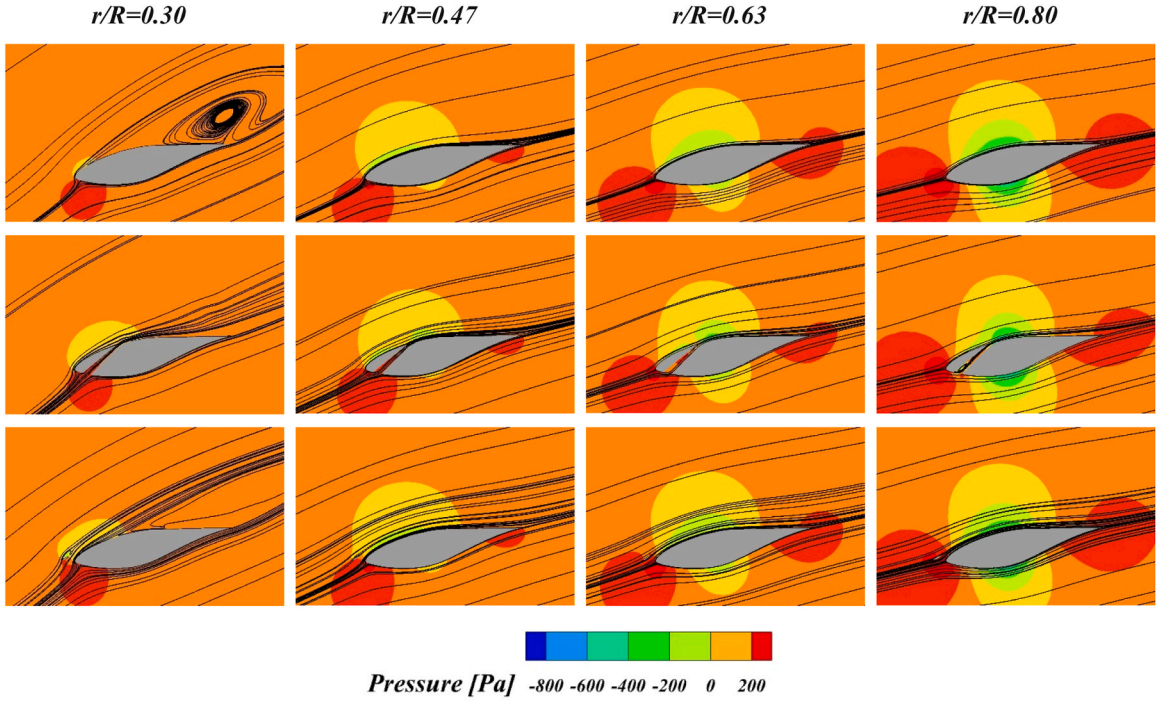

Fig. 10. Spanwise sections of streamline distribution and pressure contours comparison at U = 7 m/s for the baseline (upper), slot (middle), and slat (lower) configurations.

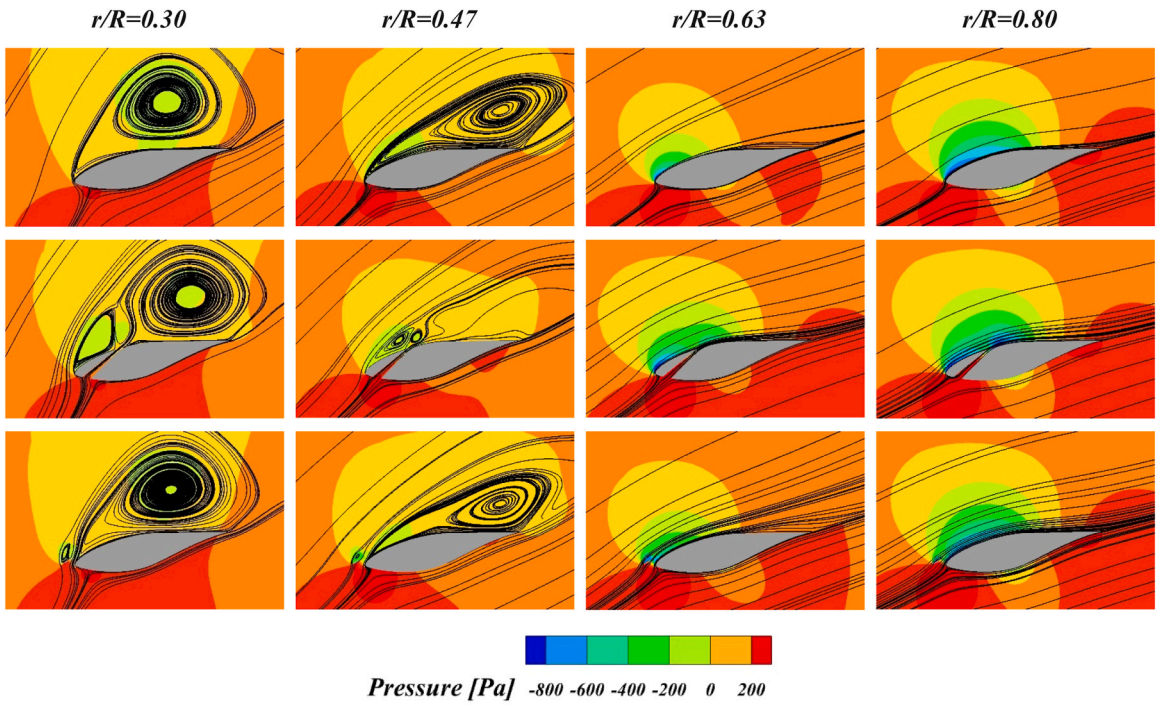

Fig. 11. Spanwise sections of streamline distribution and pressure contours comparison at U = 13 m/s for the baseline (upper), slot (middle), and slat (lower) configurations.

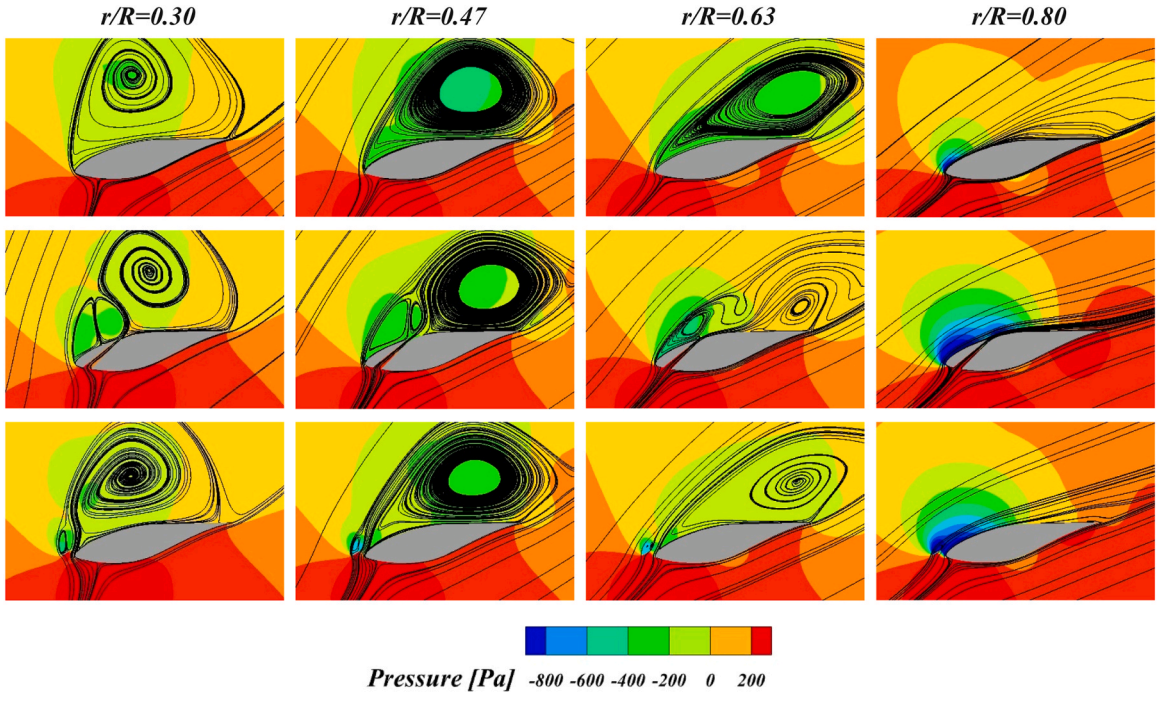

Fig. 12. Spanwise sections of streamline distribution and pressure contours comparison at U = 19 m/s for baseline (upper), slot (middle), and slat (lower).

= 0.47, both control methods exhibit significant improvement. The streamlines over the baseline and the slat's case are similar; however, we noticed a slightly more significant zone of low pressure on the suction side of the slatted case, meaning a higher fluid velocity. The slot configuration nearly eliminates separation behind the jet exit, leaving only a minor recirculation bubble near the leading edge. The flow remains mostly attached in the slat case, aided by the high-velocity stream passing through the gap between the slat and the main blade. This helps mitigate separation by energizing the boundary layer.

The flow is fully reattached at further spanwise positions (r/R = 0.63 and 0.80), and both control methods increase the extent of low-pressure zones on the suction side. These pressure contours suggest improved lift generation and boundary layer stability over the upper blade surface.

At the highest inflow velocity of 19 m/s (Fig. 12), the baseline case experiences severe separation, with flow completely detached from the surface and swept downstream at r/R= 0.30 and 0.47. Under these

extreme conditions, both control methods lose effectiveness. The slot has a modest impact at r/R = 0.63, helping redirect the separated flow toward the blade surface downstream of the jet exit. However, a recirculation zone remains near the trailing edge. The slat configuration is less effective in this regime, with only minor modifications to the suction-side pressure contours, indicating limited flow reattachment.

At r/R = 0.80, the baseline flow is reattached, and the slot and slat primarily influence the leading-edge pressure distribution. The slot's converging geometry accelerates the jet flow, creating a localized low-pressure zone at the exit. In contrast, the slat enhances flow acceleration through the gap between its profile and the main blade, strengthening the suction effect and helping to oppose adverse pressure gradients. These aerodynamic modifications enhance energy recovery in regions where the flow remains marginally attached.

Additionally, the observed flow field is dictated by the variation of the spanwise angle of attack, the wind's relative velocity amplitude changes, which induce a modification of the local Reynolds number. The constant rpm and increase of the fluid spanwise velocity induce higher Reynolds numbers and lower angles of attack towards the tip, resulting in attached flow. Overall, the performance and flow control effectiveness of both devices vary significantly with inflow velocity and spanwise position. The slot demonstrates superior control at moderate speeds and mid-span regions, while the slat primarily enhances suction effects near the leading edge.

The development of vortical structures over the blade suction surface for the baseline and controlled configurations at a velocity of 13 m/s is illustrated in Fig. 13. In the baseline case, strong three-dimensional separation vortices form between the blade root and mid-span, indicating a large region of flow detachment. When the slot is introduced, it effectively divides the separated flow into two distinct vortical structures, thereby reducing the extent of the separation zone in both chordwise and spanwise directions. In contrast, the slat configuration primarily reduces the chordwise size of the detached flow, although the spanwise coverage still extends up to mid-span.

Velocity gradients along the blade suction surface are examined to further investigate separation behavior. Negative velocity gradient values indicate adverse pressure gradient effects and potential flow reversal, typical signs of boundary layer separation. A comparative analysis of chordwise velocity gradients at selected spanwise stations (r/R=0.3, 0.47, and 0.63) is performed, as shown in Fig. 14, based on the flow features previously observed in Figs. 10–12.

- At r/R= 0.3, U = 7 m/s (Fig. 14a): The baseline configuration shows slightly negative velocity gradients near the leading edge, indicating the onset of mild separation. In contrast, both the slot and slat configurations maintain attached flow for x/C ≤ 0.2. The slot jet, in particular, exhibits strong positive velocity gradients at the exit location, reflecting an increase in fluid kinetic energy. Although velocity gradients decrease along the chord due to adverse pressure effects, they remain above the separation threshold, indicating effective suppression of separation.
- At r/R= 0.47, U = 13 m/s (Fig. 14b): Flow separation is significantly more pronounced. Both the baseline and slat cases show fully separated flow across the entire chord. However, in the slot configuration, although separation initiates before the slot, the energized jet at the exit successfully reattaches the flow and maintains attachment until the trailing edge, confirming the results from Fig. 11.
- At r/R= 0.63, U = 19 m/s (Fig. 14c): For both baseline and slat cases, velocity gradients remain negative throughout the chord, indicating complete separation. The slot configuration, however, sustains attached flow between x/C= 0.4 and x/C= 0.6, about 20 % of the chord length, resulting from the slot jet's energizing effect. Beyond this region, the gradient again falls below the separation line, suggesting the onset of a trailing recirculation bubble, as seen in Fig. 12.

These results confirm that the slot configuration consistently outperforms the slat in reattaching flow and reducing the size of the separated region, especially under moderate inflow conditions. While beneficial at lower speeds, the slat is less effective in high-separation regimes.

3.3.2. Performance evaluation

Beyond the aerodynamic flow-control benefits discussed previously, the influence of the slot and slat configurations on turbine power output and thrust force is quantitatively assessed relative to the baseline rotor at three inflow velocities (U = 7, 13, and 19 m/s) using the MRF method. The results are presented in Fig. 15.

At a velocity of 7 m/s, both control methods exhibit a lower power output than the baseline. The slot configuration yields a dramatic power drop of −72 %, while the slat shows a modest decrease of −5.32 %. This performance loss is primarily due to increased drag from both devices, especially the slot, and to limited lift generation at low wind speeds. The slat's relatively better performance stems from its ability to generate some lift enhancement across the span despite the added drag. Given that the NREL S809 Phase II rotor is based on a lift-driven S809 airfoil, the overall impact is directly proportional to the control method's aerodynamic efficiency and influence.

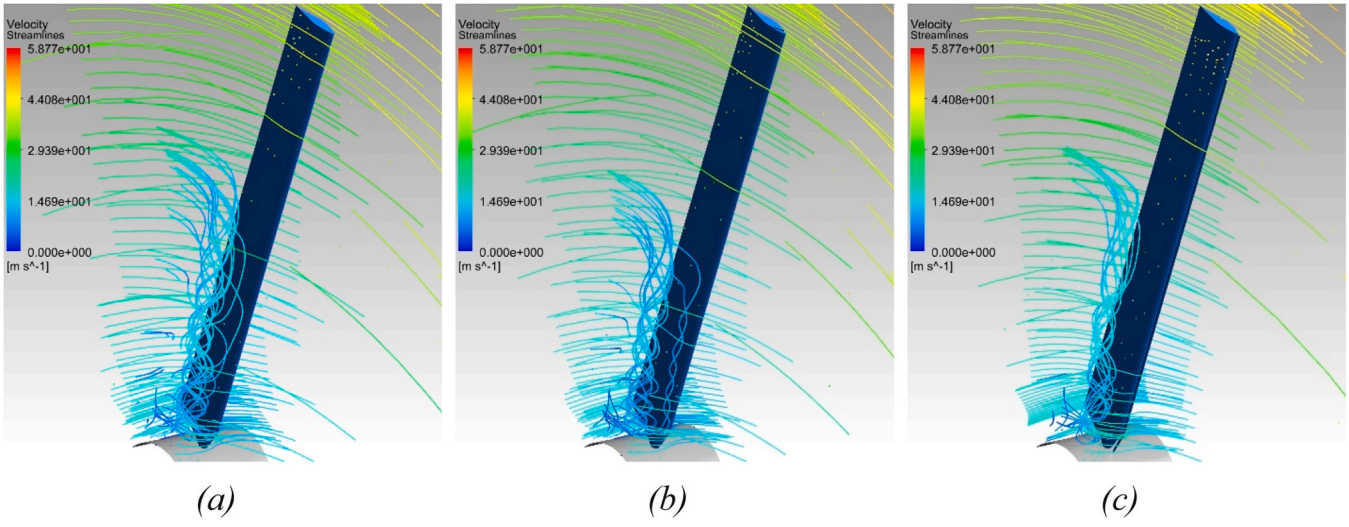

Fig. 13. Distribution of velocity Streamline around the blade suction surface; (a) baseline, (b) slot, (c) slat for U= 13 m/s.

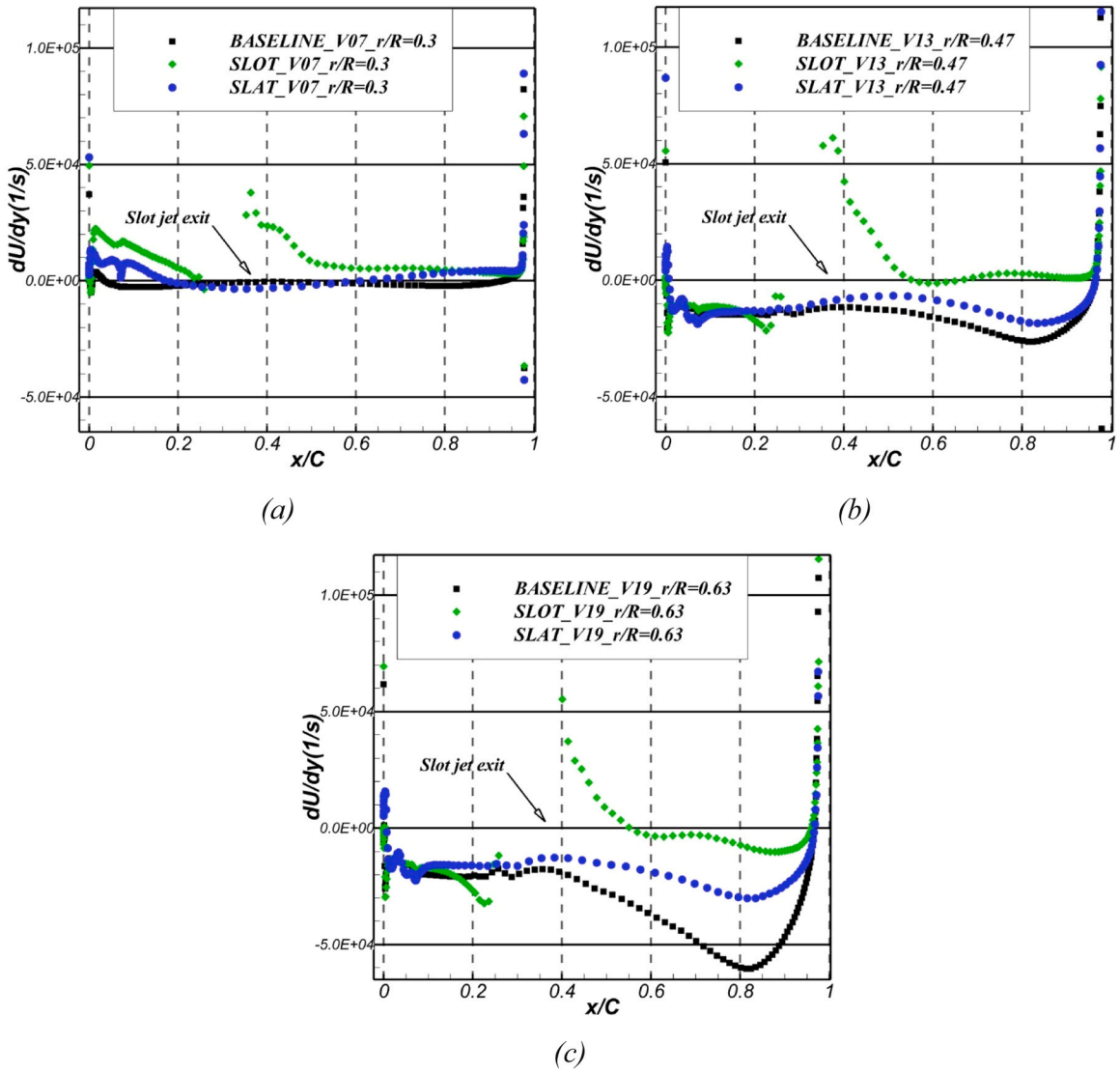

Fig. 14. Chordwise velocity gradients distribution comparison for baseline and controlled cases at (a) Inflow velocity U= 7 m/s at r/R= 0.3, (b) Inflow velocity U= 13 m/s at r/R= 0.47, and (c) Inflow velocity U= 19 m/s at r/R= 0.63.

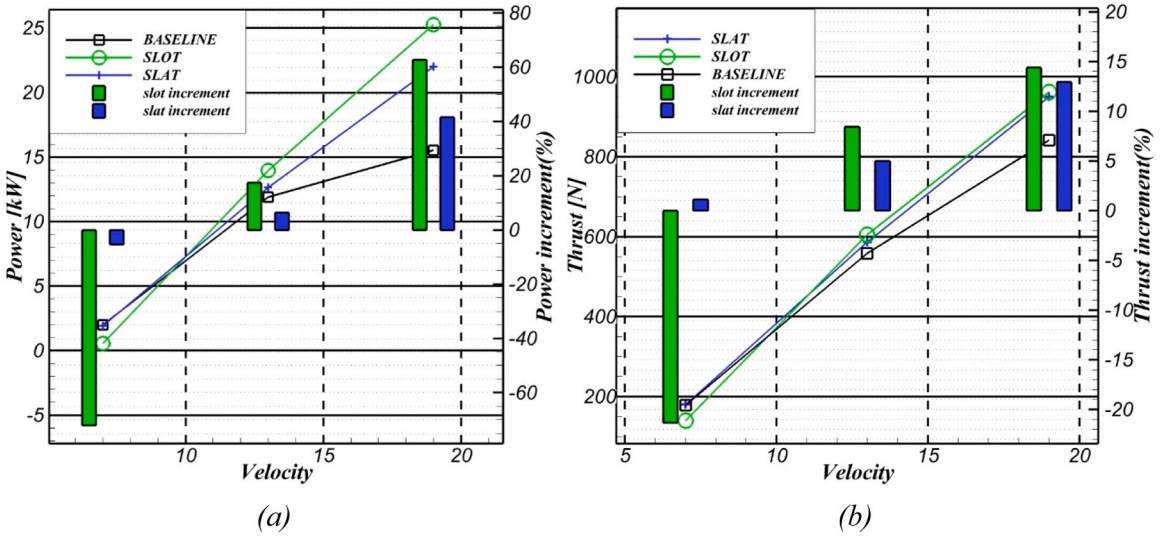

Fig. 15. Steady controlled cases comparison to baseline at U= 7, 13, and 19 m/s for (a) Produced power & power increment and (b) Thrust force & thrust increment.

At a velocity of 13 m/s, a notable shift occurs. The slot configuration achieves a power gain of + 17.41 %, while the slat yields a + 6.34 % increase. These gains align with the effective flow separation suppression observed in Fig. 11, particularly at the mid-span sections (e.g., r/R = 0.47), where both devices successfully reattach the flow and enhance the aerodynamic loading.

At a velocity of 19 m/s, the control methods deliver substantial performance improvements. The slot configuration increases power output by + 62.7 % and the slat by + 41.61 % compared to the baseline. Although the steady-state flow visualizations in Fig. 12 show noticeable regions of flow detachment across all configurations, the corresponding power values provide a more sensitive and integrated measure of separation severity. The superior performance of the slot under high inflow conditions confirms its enhanced ability to sustain overall flow attachment and delay large-scale separation, primarily by improving attachment at the rotor's outer part, thereby generating higher lift and improving the rotor's global aerodynamic efficiency.

Fig. 15b presents the evolution of thrust force, a key indicator of the axial force generated by pressure differences across the rotor. At 7 m/s, the slot reduces thrust by −21.3 %, whereas the slat has a negligible effect (+1.1 %), again reflecting their aerodynamic influence at low Reynolds numbers. At 13 m/s, both control methods increase thrust by + 8.4 % for the slot and + 5.4 % for the slat. At 19 m/s, the increases are + 14.3 % and + 12.9 %, respectively.

These performance variations demonstrate how flow modifications induced by the control methods affect sectional lift and drag, resulting in significant changes in rotor torque and axial thrust. The slot configuration proves more effective, particularly at higher speeds, due to its localized momentum injection and efficient suppression of flow detachment over critical sections of the blade span.

3.4. Unsteady SMM results

This section presents and discusses the results obtained from transient simulations using the SMM approach at an inflow velocity of U = 13 m/s, comparing the aerodynamic performance of the baseline and controlled cases (slot and slat configurations).

3.4.1. Validation of transient results

The SMM method is a time-accurate approach that resolves the dynamic interaction between rotating and stationary domains. Due to the complex nature of the mesh interfaces and strict requirements for numerical stability, model validation is essential.

To ensure the reliability of the transient simulation, the computed average torque from the SMM simulation for the baseline case is compared to the experimental data of Butterfield et al. [7] and numerical results from Sorensen & Michelsen [34]. As shown in Fig. 16, the time evolution of torque exhibits a clear periodic pattern after the initial transient, which was initialized using the steady-state solution.

The mean torque predicted by the SMM model deviates only 2.50 % and 5.87 % from the numerical and experimental values, respectively. These errors fall within acceptable margins, confirming that the unsteady simulation produces trustworthy and consistent results.

3.4.2. Performance evaluation

Following validation, the SMM method is applied to the slot and slat configurations to evaluate their unsteady power generation performance over 3.5 full rotor revolutions. The instantaneous mechanical power generated by each blade is calculated as:

$$P_T = T \cdot \Omega \cdot n$$

where P_T is the power generated from the whole turbine, T is the torque generated from one blade $[N \cdot m]$, Ω is the rotational velocity in $[rad/s]$, and n is the number of blades.

Fig. 17 shows the time evolution of the total mechanical power for the baseline, slat, and slot configurations. After discarding the initial transient peaks (due to the ramp-up from steady-state conditions), a stable periodic power pattern is observed in all three cases.

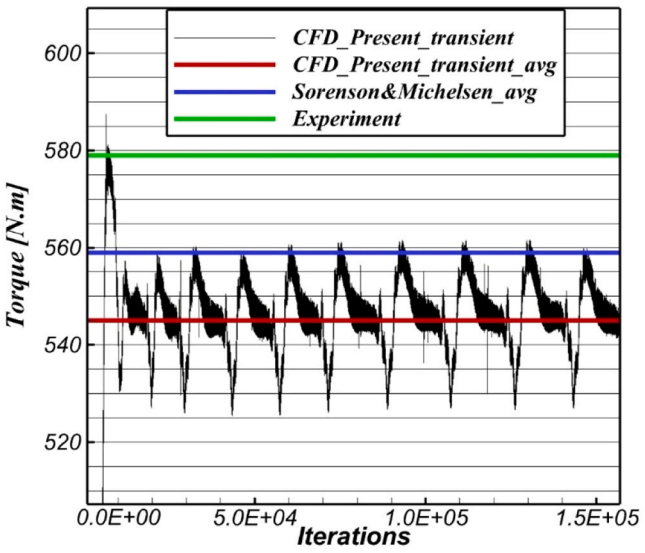

Fig. 16. Validation of SMM simulation via unsteady torque average values comparison with results of [34] and experiment.

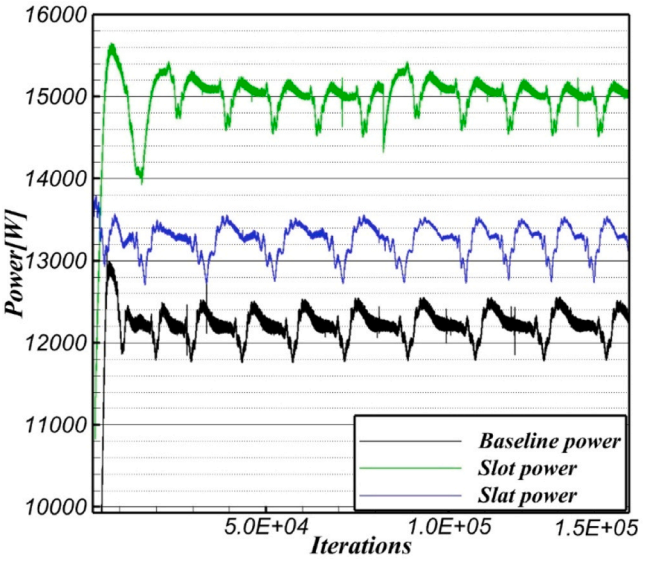

Fig. 17. Comparison of unsteady mechanical power evolution generated by baseline and controlled cases using SMM.

The average power output was computed using values after 20,000 iterations, ensuring statistical convergence. The results reveal that:

- The baseline configuration produced an average power of 12.17 kW.
- The slat configuration increased average power output to 13.24 kW, representing an improvement of + 8.74 %.
- The slot configuration yielded the highest average power, 14.74 kW, corresponding to a 21.07 % performance gain over the baseline.

These results are consistent with the steady-state observations, confirming the slot configuration's superior separation control and aerodynamic efficiency, especially under dynamic inflow conditions.

3.4.3. Flow visualization

The Q-criterion introduced by Hunt et al. [18] is used to characterize the development of vortical structures and turbulence features over the rotor. This method identifies regions where the vorticity magnitude exceeds the strain rate, indicating the presence of coherent vortex structures. The Q-criterion is defined as:

$$Q = \frac{1}{2}\left[\| \Omega\|^2 - \| S\|^2 \right]$$

The formulation of the Q-criterion is based on the velocity gradients of the stress tensor component $\frac{\delta u_i}{\delta x_j}$, and represents a balance between the rotation rate Ω and the strain rate S defined as the antisymmetric and symmetric tensor components by:

$$\Omega = \frac{1}{2}\left[\frac{\delta u_i}{\delta x_j} - \frac{\delta u_j}{\delta x_i}\right], \quad S = \frac{1}{2}\left[\frac{\delta u_i}{\delta x_j} + \frac{\delta u_j}{\delta x_i}\right]$$

A positive value of Q identifies vortex-dominated regions, while negative values correspond to strain-dominated flow.

Fig. 18 displays Q-criterion isosurfaces (Q = 0.5) colored by instantaneous velocity magnitude, highlighting vortical structures in both the near wake and over the suction side of the blade for the baseline, slot, and slat configurations.

- Fig. 18a–c illustrate the whole rotor wake structure for the three configurations.
- Fig. 18d–f provide a focused view of the blade suction side and tip regions, where flow separation and tip vortices are most pronounced.

Baseline Case (Fig. 18a, d): The baseline configuration shows significant turbulent activity, mainly originating from the blade root and suction side. A significant separation region with multiple rolled-up vortical layers is evident near the leading edge. These vortices extend well into the rotor wake and cover over half the blade span, indicating inefficient flow attachment and severe separation.

Slot Case (Fig. 18b, e): The slot configuration shows markedly improved flow control. The extent of the separation region is significantly reduced both chordwise and spanwise, especially near the blade root. A clear high-velocity stream emerges from the slot exit, energizing the boundary layer and delaying separation. The turbulent structures in the wake are less intense and more organized, indicating improved aerodynamic performance and reduced vortex-induced drag. Compared to the baseline and slat cases, the slot suppresses leading-edge vortex shedding and stabilizes the flow near the tip region.

Slat Case (Fig. 18c, f): The slat configuration induces similar vortex shedding near the root, with additional turbulent structures convected from the slat's suction side. These structures merge with the main blade's flow, contributing to the transfer of kinetic energy but not significantly reducing the spanwise extent of separation. The presence of the slat alters the local velocity distribution, but detached eddies persist, particularly in the mid-span and tip regions.

The Q-criterion analysis confirms that:

- The baseline blade suffers from severe separation and unsteady vortex shedding.
- The slat modifies the pressure field but does not fully mitigate separation, especially at the root.
- The slot provides the most effective control by reducing turbulent structures and energizing the boundary layer, enhancing aerodynamic stability and power extraction.

3.4.4. Skin friction and strain rate distribution

Skin friction is a key indicator of boundary-layer behavior and is vital for identifying attachment and separation zones. In particular, the skin friction coefficient drops to zero in regions where the boundary layer separates from the surface, reflecting the detachment of fluid particles due to adverse pressure gradients and viscous dissipation.

Fig. 19 illustrates the contours of the skin friction coefficient over the blade's suction surface for the baseline, slot, and slat configurations. The focus on the suction surface is justified by its critical role in separation-related phenomena under aerodynamic loading.

Baseline Case (Fig. 19a): Two primary zones of low skin friction are observed: A root region extending to about 25 % of the blade span near the leading edge indicates an early onset of separation. A large detachment region originates from the mid-chord and extends toward the trailing edge, with axial and radial elongation driven by centrifugal pumping and Coriolis effects. These forces act to redistribute the flow radially and chordwise, contributing to the flow instability and vortex shedding.

Slot Case (Fig. 19b): The slot significantly alters the distribution of skin friction. A distinct, elongated, low-friction region extends across half the span at the trailing edge. The root separation zone is also fragmented and less severe, suggesting improved flow stability. The jet from the slot exit increases Coriolis-induced tangential forces, resulting in a more two-dimensional flow that enhances attachment and delays separation.

Slat Case (Fig. 19c): The presence of the slat above the leading edge slightly modifies the root separation region, reducing its severity. This is attributed to the accelerated flow in the gap between the slat's trailing edge and the blade's leading edge, which re-energizes the boundary layer. However, the tip separation region is extended and appears more pronounced than in the baseline case, likely due to increased drag and surface curvature effects.

The instantaneous strain rate is closely related to turbulence generation and aeroacoustic noise. High-strain-rate regions promote the formation of vortices, energy redistribution, and pressure fluctuations, making this a crucial metric in both aerodynamic and aeroacoustic analysis [1].

Fig. 20 displays normalized strain-rate contours over the blade's suction surface for the baseline, slot, and slat cases. The normalization factor used is c/U2, where c is the chord length, and U is the inflow velocity.

Baseline Case (Fig. 20a): Strain rate is moderate near the root, reflecting dominant separation and weak shear. It gradually increases toward the mid-span and tip regions, following the increase in velocity and shear forces induced by rotation. However, chordwise strain generally decreases toward the trailing edge due to detachment and reduced momentum.

Slot Case (Fig. 20 b): The strain field is clearly modified. The strain rate is higher in regions surrounding the slot exit, indicating enhanced momentum and shear due to re-energized flow. Spanwise, the high-strain zones are more extended, particularly in the mid-span, where the slot's control effect is most pronounced. These findings are consistent with prior flow-visualization and skin-friction results.

Slat Case (Fig. 20c): The strain rate distribution is similar to the baseline, with only minor variations along the span. This suggests that the slat has limited influence on modifying strain behavior and turbulent shear development.

3.4.5. Vorticity and wake topology

Fig. 21 presents instantaneous vorticity magnitude contours on four downwind vertical planes located at different streamwise positions: y/R = 0.02, 0.03, 0.04, and 0.05. The visualization focuses on the upper part of the blade near the tip region, capturing the development and dissipation of vortical structures shed by the rotor in the near wake, with particular emphasis on the tip vortex. In the baseline case, strong and disorganized vortical structures persist downstream, particularly in the root and mid-span regions. The slot case exhibits a more organized wake with reduced vorticity intensity and narrower shedding structures, confirming its efficiency in limiting separation and suppressing turbulence. In contrast, the slat case retains substantial vortex intensity, resembling the baseline in many respects, particularly near the tip.

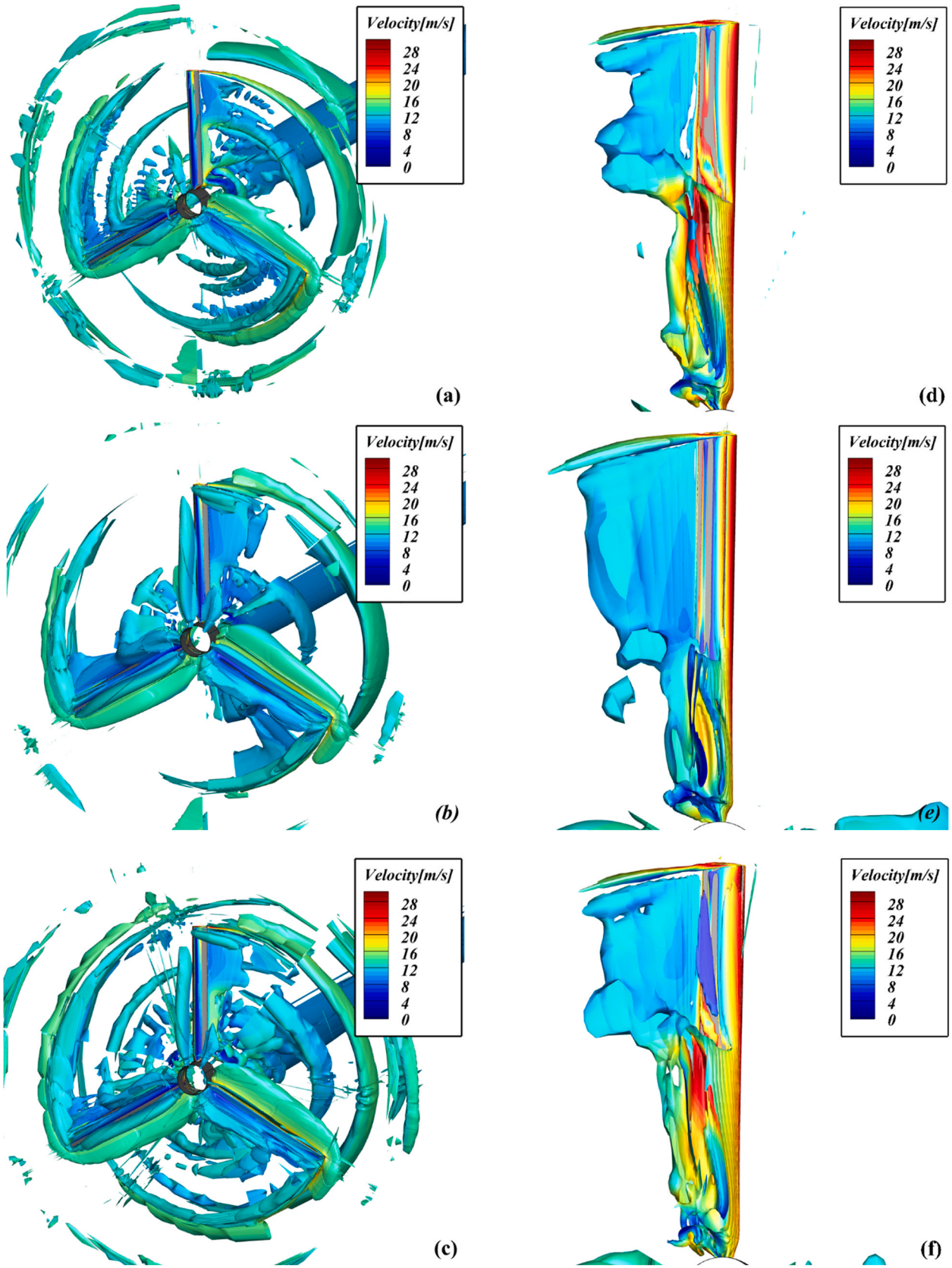

Fig. 18. Isosurfaces of Q-criterion (Q=0.5) colored by instantaneous velocity magnitude for the whole turbine (a) baseline, (b) slot, (c) slat, and suction side view (d) baseline, (e) slot, (f) slat.

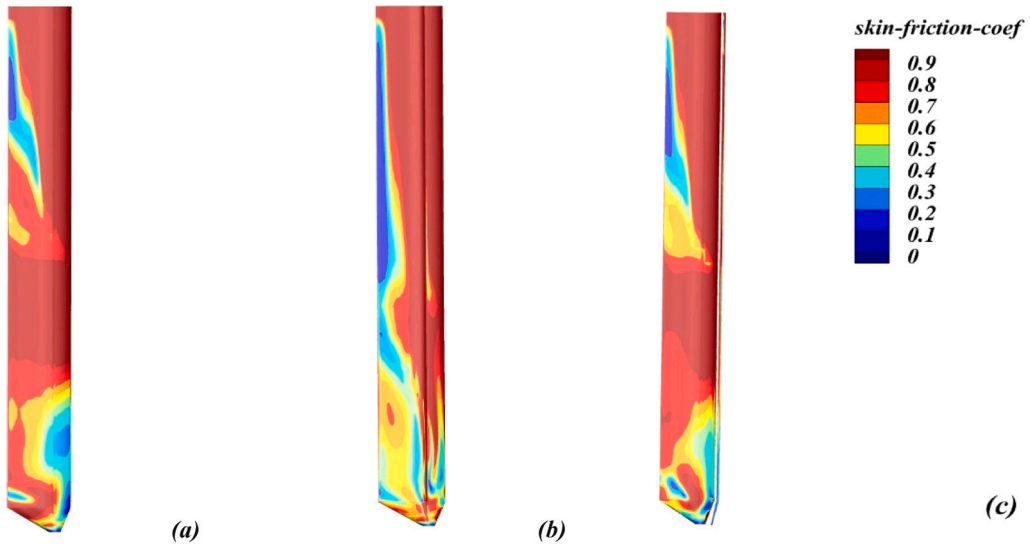

Fig. 19. Skin friction coefficient contours over the blade suction surface (a) baseline, (b) slot, (c) slat.

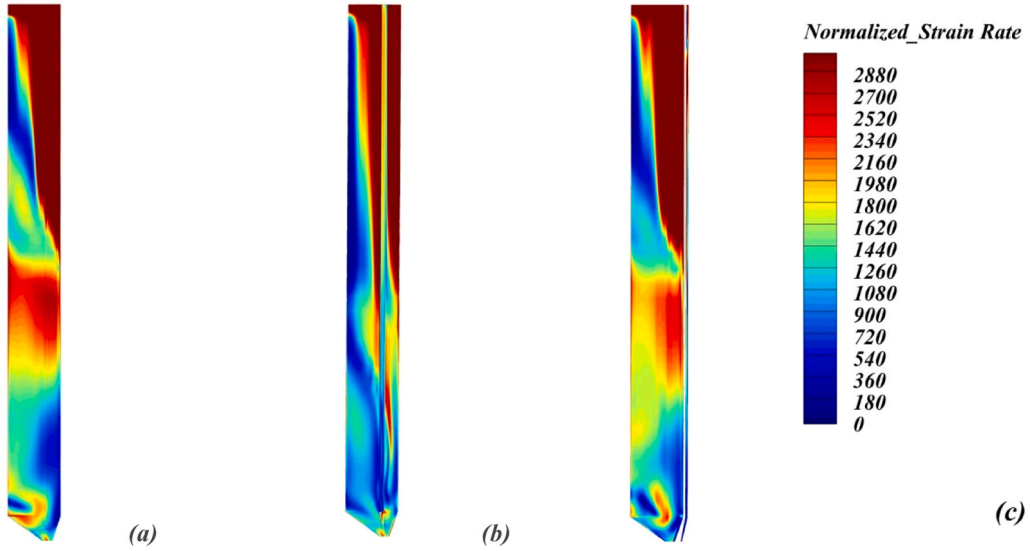

Fig. 20. Contours of the instantaneous rate of strain normalized by the [rate of strain $\left(\frac{c}{U^2}\right)$] over the blade suction surface: (a) baseline, (b) slot, (c) slat.

3.5. Far-field noise and directivity

To evaluate the aeroacoustic impact of implementing passive flow control methods on the S809 Phase II rotor, far-field sound pressure levels (SPL) were computed from unsteady SMM simulation results. The (FW-H) acoustic analogy was employed to capture pressure perturbations originating from surface flow dynamics.

According to IEC 61400–11 standards, the primary far-field receiver was placed downwind at a distance of H + D/2, where H is the tower height, and D is the turbine diameter. All solid, no-slip surfaces, including the slat suction and pressure surfaces and the internal walls of the slot, were treated as noise sources. The unsteady pressure fluctuations were collected during the last rotor revolution to ensure fully developed flow and acoustics. The resulting acoustic signal was processed using the Fast Fourier Transform (FFT) to generate the SPL in the frequency domain. A reference pressure level of $P_{ref} = 2 \times 10^{-5}$ Pa was used, and the analysis was conducted over a frequency range of 1 Hz to 1 kHz.

Additionally, 36 ground-level receivers were placed in a polar configuration around the turbine at a D radius, enabling directivity analysis at discrete frequency bands.

Fig. 22 presents the SPL spectra measured at the main receiver location for the baseline, slot, and slat configurations:

- Below 4 Hz, the baseline values are lowest, with both the slot and slat cases showing almost identical SPL levels.
- For frequencies below 17 Hz, the baseline turbine consistently exhibits the highest SPL, suggesting greater low-frequency noise generation without flow control.
- The slot and slat configurations yield reduced SPLs at very low frequencies, indicating effective damping of large-scale pressure fluctuations typically associated with separated flow.
- Between 10 Hz and 100 Hz, all three configurations exhibit irregular small-scale fluctuations without dominant tonal components. These variations are interpreted as statistical scatter in the spectral estimate, arising from the finite time series length and the broadband nature of the signal. No specific physical mechanism is therefore assigned to this frequency band, and the discussion focuses instead

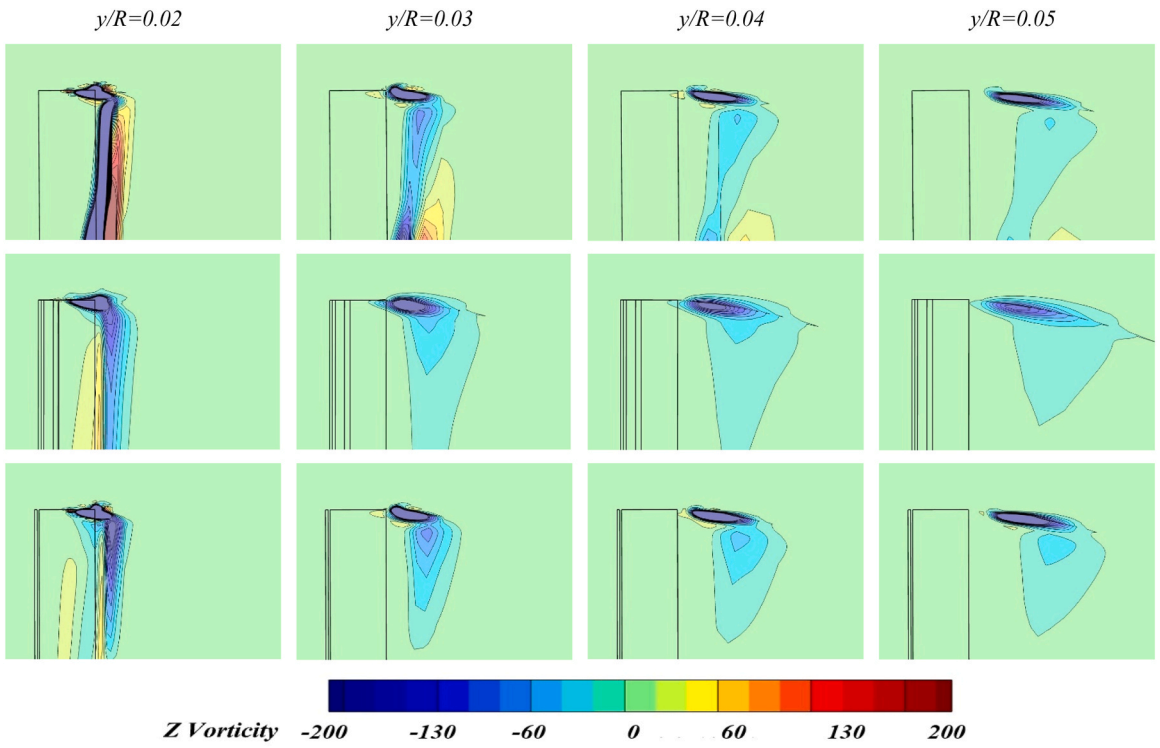

Fig. 21. Instantaneous vorticity magnitude contours on four downwind vertical planes located at different streamwise positions: y/R = 0.02, 0.03, 0.04, and 0.05 for baseline (upper), slot (middle), and slat (lower).

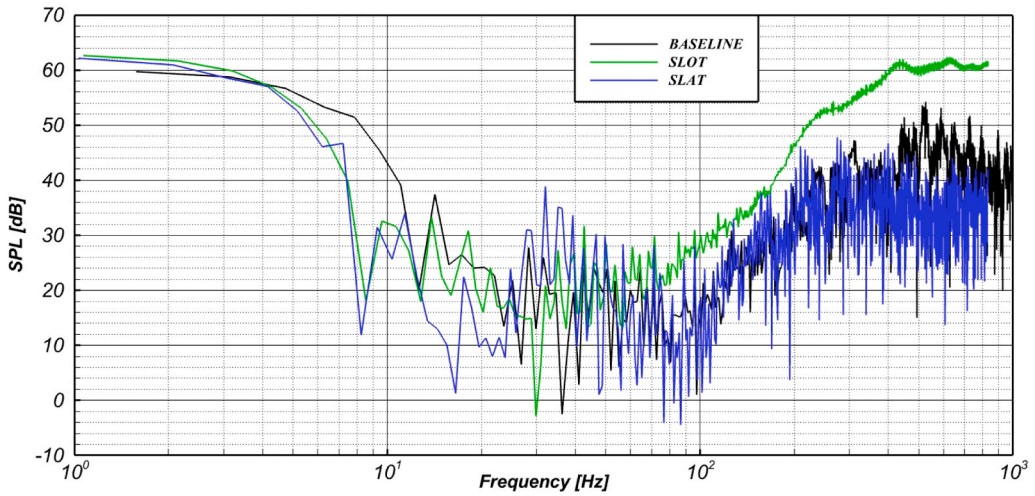

Fig. 22. Sound pressure level at H+D/2 receiver for baseline and passive control cases.

on the low-frequency (<10–20 Hz) and high-frequency (~1 kHz) ranges where clearer trends between configurations emerge.

- Beyond 100 Hz, the baseline and slat SPL curves converge and remain comparable across the mid-frequency range.
- At high frequencies (near 1 kHz), the slot configuration exhibits a peak SPL approximately 20 dB higher than the baseline and slat cases. This increased noise emission is likely linked to enhanced aerodynamic loading, higher local shear, and the presence of fine-scale vortical structures, particularly in the blade tip and trailing edge regions, as observed in Q-criterion visualizations (Fig. 18e).

Although the slat exhibits higher SPLs than the baseline at isolated frequency bands, its smaller surface area ratio (c/C = 0.05) limits its acoustic impact at high frequencies. In contrast, the slot's convergent geometry promotes flow suction on the pressure side and ejection on the suction side, thereby enhancing shear and turbulence, key contributors to aerodynamic noise generation. The characteristic cavity shape of the slot is primarily responsible for the previously discussed acoustic emissions [17].

Fig. 23 illustrates polar directivity patterns at four selected frequencies, 125 Hz, 250 Hz, 500 Hz, and 1 kHz, to further characterize the directional distribution of noise.

At 125 Hz and 250 Hz, the baseline and slat cases show clear dipolar radiation patterns, with peak lobes oriented at approximately 120° and 240°. These patterns reflect the typical low-frequency vortex shedding and loading noise associated with rotating blades. In contrast, the slot configuration exhibits a more omnidirectional radiation pattern at 125 Hz. It shifts its peak radiation to 90° and 270° at 250 Hz, likely due

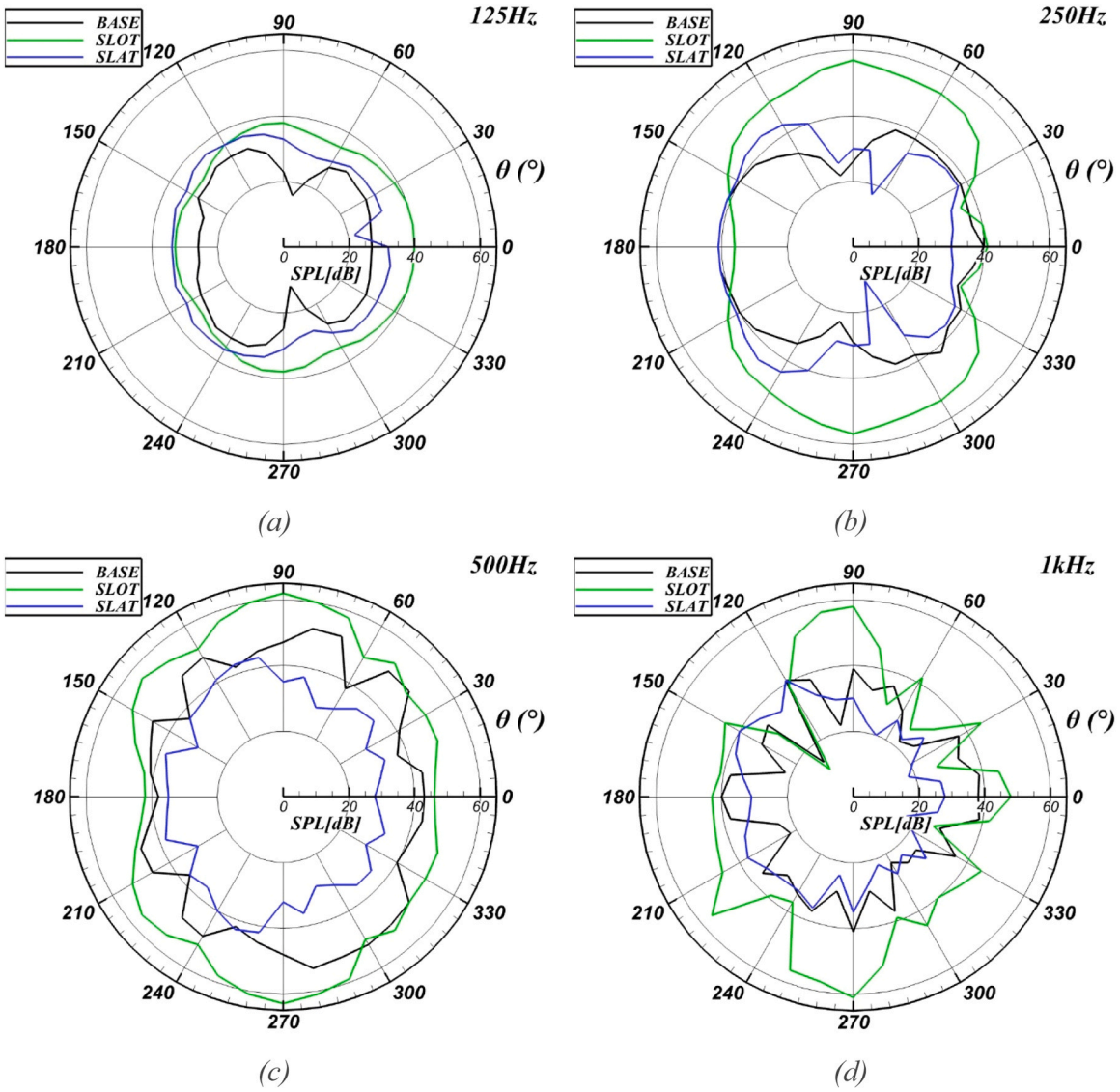

Fig. 23. Directivity comparison for baseline and passive control cases at frequency ranges of: (a) 125 Hz, (b) 250 Hz, (c) 500 Hz, (d) 1 kHz.

to flow jet interactions altering vortex trajectories. At 500 Hz, the baseline maintains dominant radiation in all quadrants compared to the slat. At the same time, the slot configuration surpasses both, producing SPL peaks 10–20 dB higher, particularly along the crosswind directions (90° and 270°). At 1 kHz, all three configurations show complex, multi-lobed patterns. The slot configuration exhibits two pronounced peaks at 90° and 270°, with SPLs up to 20 dB higher than the baseline and the slat.

Overall, both passive control methods contribute to noise reduction at very low frequencies, thereby supporting their benefits for mitigating low-frequency noise. However, the slot configuration exhibits notable high-frequency noise amplification, which should be considered when evaluating the trade-off between aerodynamic performance gains and acoustic emissions. Although less effective in noise suppression, the slat provides a more balanced aeroacoustic behavior, especially in environments with stricter noise constraints.

4. Conclusions

This study presents a comprehensive numerical investigation of two previously validated 2D passive flow-separation control devices, a slat and a slot, implemented on the entire 3D rotor of the NREL S809 Phase II small-scale HAWT. The research evaluates aerodynamic performance, flow control effectiveness, and acoustic behavior across various operating conditions using both steady-state (MRF) and unsteady-state (SMM) simulation approaches, coupled with the RANS K-ω SST turbulence model.

A structured multi-block mesh and a robust simulation strategy enabled accurate capture of complex flow dynamics and noise radiation characteristics. Notably, this work represents one of the few studies to extend 2D-validated flow-control methods to a complete 3D rotating-blade configuration, offering new insights into their aerodynamic and aeroacoustic implications.

The following key findings and contributions are emphasized:

1. Steady-State (MRF) Analysis at U = 7, 13, and 19 m/s:

- Severe flow separation is observed on the inboard blade sections, especially at higher wind speeds.
- The slat mitigates separation by generating an energized shear layer between its trailing edge and the blade's leading edge and convecting high-momentum flow over the suction side.
- With its converging nozzle geometry, the slot effectively injects high-velocity flow to counter adverse pressure gradients and delay separation. The spanwise flow topology is shaped by variations in local

angle of attack and fluctuations in the Reynolds number, driven by changes in relative velocity across radial positions. Both the slot and the slat are least effective near the root region, and the slot, in particular, induces power penalties at a wind speed of 7 m/s.

- In terms of total turbine power output:

- At 7 m/s, the slat shows minimal penalty (−5.32 %), while the slot suffers a −72 % drop.
- At 13 m/s, the slot yields a 17.41 % power gain, outperforming the slat's 6.34 %.
- At 19 m/s, both methods significantly improve power: + 62.7 % (slot) and + 41.6 % (slat), reflecting successful control of high-speed separation.

2. Unsteady (SMM) Analysis at U = 13 m/s:

- The slot increases the unsteady average power output by 21.07 %, compared to 8.74 % for the slat.
- In terms of flow behaviour, the Q-criterion visualizations show that both methods alter vortex topology: the slat enhances tip and root vortex shedding, while the slot suppresses near-field turbulence and streamlines vortex structures.
- Skin friction analysis confirms the slot's ability to re-energize boundary layer flow, reducing the extent of detachment zones and promoting more 2D-like flow, especially near the trailing edge.

3. Aeroacoustic Analysis Using FW-H Analogy:

- Both control methods reduce noise at low frequencies (<17 Hz) compared to the baseline.
- In the mid-frequency range (10–100 Hz), oscillatory SPL patterns are observed, with the slot maintaining lower amplitudes.
- At high frequencies (~1 kHz), the slot generates up to 20 dB more noise than the baseline due to increased aerodynamic loading and tip-vortex activity.
- Directivity patterns show that the slot produces omnidirectional radiation at mid-frequencies and pronounced multi-lobed emissions at 1 kHz, with increases of up to 20 dB at the 90° and 270° receiver positions. The slot's cavity-like geometry contributes to noise generation, though it can also reduce noise at specific isolated frequencies. The slat, as expected, contributes to the overall acoustic emission by generating additional surface noise from its aerodynamic body.

The main contributions of this research are:

- This work is among the first to implement and analyze 3D versions of slat and slot flow control devices on a rotating HAWT blade, going beyond previous 2D parametric studies.
- It combines a detailed assessment of the aerodynamic flow field with comprehensive aeroacoustic analysis using the FW-H analogy, thereby offering a multidisciplinary perspective on flow control effectiveness.
- The study also identifies trade-offs between performance enhancement and noise generation, highlighting the need to balance aerodynamic gains with the environmental impact of noise.

Given that control-induced noise penalties can be significant, especially at high frequencies, when applied to large-scale turbines, future research should: 1) extend the present methodology to MW-class wind turbines using high-fidelity turbulence models (e.g., DES, LES); 2) Investigate combined passive control strategies (e.g., slat + slot) on more complex geometries, such as the NREL S809 Phase VI; 3) Explore geometry optimization of flow control devices to maximize power gain while minimizing acoustic emissions.

Finally, the authors acknowledge that RANS capabilities in computational aeroacoustics studies and data-sampling considerations related to time-series length and sampling rate are the main limitations in a limited transient simulation time. These factors can influence the quality of the acoustic data presented in the present study, and better estimates would be achievable with a high-fidelity LES model and increased simulation time.

CRediT authorship contribution statement

Adrian Ilinca: Writing – review & editing, Supervision, Methodology, Formal analysis. **Abdelouaheb Djemili:** Writing – original draft, Supervision, Resources, Investigation, Funding acquisition, Formal analysis. **Riyadh Belamadi:** Writing – original draft, Validation, Supervision, Software, Methodology, Investigation, Conceptualization. **Sami Bouterra:** Writing – original draft, Visualization, Validation, Methodology, Investigation, Formal analysis, Conceptualization.

Declaration of Competing Interest

The authors declare that they have no known competing financial interests or personal relationships that could have appeared to influence the work reported in this paper.

Data Availability

Data will be made available on request.

References

[1] M.Z. Akhter, A.R. Ali, H.K. Jawahar, F.K. Omar, E. Elnajjar, Performance enhancement of small-scale wind turbine featuring morphing blades, Energy 278 (2023) 127772, https://doi.org/10.1016/j.energy.2023.127772.
[2] A.R. Ali, M.Z. Akhter, F.K. Omar, Performance enhancement of a small-scale wind turbine featuring morphed trailing edge, Sustain. Energy Technol. Assess. 46 (2021) 101229, https://doi.org/10.1016/j.seta.2021.101229.
[3] I. ANSYS, Fluent Theory guide, ANSYS Fluent Theory Guide 15 (2013) 0.
[4] R. Belamadi, A. Settar, K. Chetehouna, A. Ilinca, Numerical modeling of horizontal axis wind turbine: aerodynamic performances improvement using an efficient passive flow control system, Energies 15 (13) (2022) 4872. ⟨https://www.mdpi.com/1996-1073/15/13/4872⟩.
[5] S. Bouterra, R. Belamadi, A. Djemili, A. Ilinca, Flow separation control and aeroacoustic effects of a leading-edge slat over a wind turbine blade, Energies 17 (22) (2024) 5597. ⟨https://www.mdpi.com/1996-1073/17/22/5597⟩.
[6] T.F. Brooks, R.H. Schlinker, Progress in rotor broadband noise research, 1983.
[7] C. Butterfield, W. Musial, G. Scott, D. Simms, NREL Comb. Exp. Final Rep. phase II (1992), https://doi.org/10.2172/883861.
[8] P.K. Chang, CHAPTER I - Introduction to the Problems of Flow Separation, in: P. K. Chang (Ed.), Separation of Flow, Pergamon, 1970, pp. 1–54, https://doi.org/10.1016/B978-0-08-013441-3.50005-8.
[9] G. Chen, B. Chen, X. Yang, X. Tang, J. Ding, P. Weng, Noise reduction for high-lift devices on a swept wing model by droop nose, Aerosp. Sci. Technol. 143 (2023) 108702, https://doi.org/10.1016/j.ast.2023.108702.
[10] F. Chen, W. Zhong, D. Wan, Numerical investigation of the water entry of inclined cylinders using dynamic sliding mesh method, Ocean Eng. 257 (2022) 111525, https://doi.org/10.1016/j.oceaneng.2022.111525.
[11] T. Cho, C. Kim, D. Lee, Acoustic measurement for 12% scaled model of NREL Phase VI wind turbine by using beamforming, Curr. Appl. Phys. 10(2 Suppl.) (2010) S320–S325, https://doi.org/10.1016/j.cap.2009.11.035.
[12] G.P. Corten, Flow separation on wind turbine blades, Univ. Utrecht (2001) *733*.
[13] Duque, E., Dam, C.P. v., & Hughes, S. (n.d) Navier-Stokes simulations of the NREL Combined Experiment Phase II rotor. In 37th Aerospace Sciences Meeting and Exhibit. https://doi.org/10.2514/6.1999-37.
[14] V. Esfahanian, A. Salavati Pour, I. Harsini, A. Haghani, R. Pasandeh, A. Shahbazi, G. Ahmadi, Numerical analysis of flow field around NREL Phase II wind turbine by a hybrid CFD/BEM method, J. Wind Eng. Ind. Aerodyn. 120 (2013) 29–36, https://doi.org/10.1016/j.jweia.2013.06.006.
[15] F. Farassat, Linear acoustic formulas for calculation of rotating blade noise, AIAA J. 19 (1981) 1122–1130.
[16] B. Greschner, F. Thiele, M.C. Jacob, D. Casalino, Prediction of sound generated by a rod–airfoil configuration using EASM DES and the generalised Lighthill/FW-H analogy, Comput. Fluids 37 (4) (2008) 402–413, https://doi.org/10.1016/j.compfluid.2007.02.013.
[17] M.S. Howe, Aerodynamic sound generated by a slotted trailing edgeProc, R. Soc. Lond. (1980) A373235–A373252, https://doi.org/10.1098/rspa.1980.0146.
[18] J. C. Hunt, A. A. Wray, P. Moin, Eddies, streams, and convergence zones in turbulent flows. Studying turbulence using numerical simulation databases, 2,

Proceedings of the 1988 summer program, 1988. https://web.stanford.edu/group/ctr/Summer/201306111537.pdf.
[19] H.R. Kaviani, A. Nejat, Aerodynamic noise prediction of a MW-class HAWT using shear wind profile, J. Wind Eng. Ind. Aerodyn. 168 (2017) 164–176, https://doi.org/10.1016/j.jweia.2017.06.003.
[20] A. Khedr, F. Castellani, Critical issues in the moving reference frame CFD simulation of small horizontal axis wind turbines, Energy Convers. Manag. X 22 (2024) 100551, https://doi.org/10.1016/j.ecmx.2024.100551.
[21] S. Kim, C. Cheong, Development of low-noise drag-type vertical wind turbines, Renew. Energy 79 (2015) 199–208, https://doi.org/10.1016/j.renene.2014.09.047.
[22] M.J. Lighthill, On sound generated aerodynamically. I. General Theory, Proc. R. Soc. Lond. Ser. A 211 (1952) 564–587, https://doi.org/10.1098/rspa.1952.0060.
[23] Y. Liu, Q. Xiao, A. Incecik, C. Peyrard, D. Wan, Establishing a fully coupled CFD analysis tool for floating offshore wind turbines, Renew. Energy 112 (2017) 280–301, https://doi.org/10.1016/j.renene.2017.04.052.
[24] A. McAlpine, R.J. Astley, Aeroacoustics research in Europe: the CEAS-ASC report on 2011 highlights, J. Sound Vib. 331 (21) (2012) 4609–4628, https://doi.org/10.1016/j.jsv.2012.05.012.
[25] F.R. Menter, Two-equation eddy-viscosity turbulence models for engineering applications, AIAA J. 32 (8) (1994) 1598–1605, https://doi.org/10.2514/3.12149.
[26] Michel, U., Eschricht, D., Greschner, B., Knacke, T., Mockett, C., & Thiele, F. (2010). Advanced DES Methods and Their Application to Aeroacoustics. In {C}S.-H. Peng, P. Doerffer, & W. Haase{C}, Progress in Hybrid RANS-LES Modelling Berlin, Heidelberg.
[27] J.-O. Mo, Y.-H. Lee, Numerical simulation for prediction of aerodynamic noise characteristics on a HAWT of NREL phase VI, J. Mech. Sci. Technol. 25 (5) (2011) 1341–1349, https://doi.org/10.1007/s12206-011-0234-1.
[28] M.H. Mohamed, Aero-acoustics noise evaluation of H-rotor Darrieus wind turbines, Energy 65 (2014) 596–604, https://doi.org/10.1016/j.energy.2013.11.031.
[29] W. Mostafa, A. Abdelsamie, M. Sedrak, D. Thévenin, M. Mohamed, Quantitative impact of a micro-cylinder as a passive flow control on a horizontal axis wind turbine performance, Energy 244 (2021) 122654, https://doi.org/10.1016/j.energy.2021.122654.
[30] P.I. Muiruri, O.S. Motsamai, R. Ndeda, A comparative study of RANS-based turbulence models for an upscale wind turbine blade, SN Appl. Sci. 1 (3) (2019) 237, https://doi.org/10.1007/s42452-019-0254-5.
[31] Noise Generation, Wind Farm Noise Meas. Assess. (2017) 119–156, https://doi.org/10.1002/9781118826140.ch3.
[32] C. Paz, E. Suárez, C. Gil, J. Vence, Assessment of the methodology for the CFD simulation of the flight of a quadcopter UAV, J. Wind Eng. Ind. Aerodyn. 218 (2021) 104776, https://doi.org/10.1016/j.jweia.2021.104776.
[33] B. Riyadh, A. Djemili, A. Ilinca, M. Ramzi, Aerodynamic performance analysis of slotted airfoils for application to wind turbine blades, J. Wind Eng. Ind. Aerodyn. 151 (2016) 79–99, https://doi.org/10.1016/j.jweia.2016.01.011.
[34] Sorensen, N., & Michelsen, J. (n.d)Aerodynamic predictions for the Unsteady Aerodynamics Experiment Phase-II rotor at the National Renewable Energy Laboratory. In 2000 ASME Wind Energy Symposium. https://doi.org/10.2514/6.2000-37.
[35] J. Su, H. Lei, D. Zhou, Z. Han, Y. Bao, H. Zhu, L. Zhou, Aerodynamic noise assessment for a vertical axis wind turbine using Improved Delayed Detached Eddy Simulation, Renew. Energy 141 (2019) 559–569, https://doi.org/10.1016/j.renene.2019.04.038.
[36] M. Tabib, M.S. Siddiqui, A. Rasheed, T. Kvamsdal, Industrial scale turbine and associated wake development -comparison of RANS based Actuator Line Vs Sliding Mesh Interface Vs Multiple Reference Frame method, Energy Procedia 137 (2017) 487–496, https://doi.org/10.1016/j.egypro.2017.10.377.
[37] C. Testa, F. Porcacchia, S. Zaghi, M. Gennaretti, Study of a FWH-based permeable-surface formulation for propeller hydroacoustics, Ocean Eng. 240 (2021) 109828, https://doi.org/10.1016/j.oceaneng.2021.109828.
[38] J.M. Turner, J.W. Kim, Aerofoil dipole noise due to flow separation and stall at a low Reynolds number, Int. J. Heat. Fluid Flow. 86 (2020) 108715, https://doi.org/10.1016/j.ijheatfluidflow.2020.108715.
[39] S. Wagner, R. Bareiß, G. Guidati, Introduction to Aeroacoustics. Wind Turbine Noise, Springer Berlin Heidelberg, 1996, pp. 27–65, https://doi.org/10.1007/978-3-642-88710-9_3.
[40] Wagner, C., Hüttl, T., & Sagaut, P. (2007). Large-eddy simulation for acoustics.
[41] H. Wang, B. Chen, Investigation on aerodynamic noise for leading edge erosion of wind turbine blade, J. Wind Eng. Ind. Aerodyn. 240 (2023) 105484, https://doi.org/10.1016/j.jweia.2023.105484.
[42] S.H. Wasala, R.C. Storey, S.E. Norris, J.E. Cater, Aeroacoustic noise prediction for wind turbines using Large Eddy Simulation, J. Wind Eng. Ind. Aerodyn. 145 (2015) 17–29, https://doi.org/10.1016/j.jweia.2015.05.011.
[43] J.E.F. Williams, D.L. Hawkings, Sound generation by turbulence and surfaces in arbitrary motion. Philosophical Transactions of the Royal Society of London, Ser. A Math. Phys. Sci. 264 (1151) (1969) 321–342. ⟨http://www.jstor.org/stable/73790⟩.
[44] WWEA. (2023). WWEA Annual Report 2023: Record Year for Windpower. ⟨https://wwindea.org/AnnualReport2023⟩.